

# The relationship between $\gamma$ Cassiopeiae's X-ray emission and its circumstellar environment

M. A. Smith<sup>1</sup>, R. Lopes de Oliveira<sup>2,3</sup>, C. Motch<sup>4</sup>, G. W. Henry<sup>5</sup>, N. D. Richardson<sup>6</sup>, K. S. Bjorkman<sup>7</sup>, Ph. Stee<sup>8</sup>, D. Mourard<sup>8</sup>, J. D. Monnier<sup>9</sup>, X. Che<sup>9</sup>, R. Bücke<sup>10</sup>, E. Pollmann<sup>11</sup>, D. R. Gies<sup>6</sup>, G. H Schaefer<sup>6</sup>, T. ten Brummelaar<sup>6</sup>, H. A. McAlister<sup>6</sup>, N. H. Turner<sup>6</sup>, J. Sturmann<sup>6</sup>, L. Sturmann<sup>6</sup>, and S. T. Ridgway<sup>12</sup>

<sup>1</sup> Catholic University of America, 3700 San Martin Dr., Baltimore, MD 21218, USA  
e-mail: [msmith@stsci.edu](mailto:msmith@stsci.edu)

<sup>2</sup> Universidade Federal de Sergipe, Departamento de Física, Av. Marechal Rondon s/n, 49100-000 São Cristóvão, SE, Brazil

<sup>3</sup> Universidade de São Paulo, Instituto de Física de São Carlos, Caixa Postal 369, 13560-970, São Carlos, SP, Brazil

<sup>4</sup> Université de Strasbourg, CNRS, Observatoire Astronomique, 11 rue de l'Université, 67000 Strasbourg, France

<sup>5</sup> Center of Excellence in Information Systems, Tennessee State University, 3500 John Merritt Blvd., Nashville, TN, USA

<sup>6</sup> Center for High Angular Resolution Astronomy, Department of Physics and Astronomy, Georgia State University, PO Box 4106, Atlanta, GA 30202-4106, USA

<sup>7</sup> Ritter Astrophysical Research Center, Department of Physics & Astronomy, University of Toledo, 2801 W. Bancroft, Toledo, OH 43606, USA

<sup>8</sup> Laboratoire Lagrange, UMR 7293 UNS-CNRS-OCA, Bd de l'Observatoire, BP 4229, 06304 Nice Cedex 4, France

<sup>9</sup> Department of Astronomy, University of Michigan, Ann Arbor, MI 48109, USA

<sup>10</sup> Anna-von-Gierke-Ring 147, 21035 Hamburg, Germany

<sup>11</sup> Emil-Nolde-Str. 12, 51375 Leverkusen, Germany

<sup>12</sup> National Optical Astronomical Observatory, 950 North Cherry Ave., Tucson, AZ 85719, USA

Received 27 October 2011 / Accepted 22 January 2012

## ABSTRACT

$\gamma$  Cas is the prototypical classical Be star and is recently best known for its variable hard X-ray emission. To elucidate the reasons for this emission, we mounted a multiwavelength campaign in 2010 centered around four *XMM-Newton* observations. The observational techniques included long baseline optical interferometry (LBOI) from two instruments at CHARA, photometry carried out by an automated photometric telescope and H $\alpha$  observations. Because  $\gamma$  Cas is also known to be in a binary, we measured radial velocities from the H $\alpha$  line and redetermined its period as  $203.55 \pm 0.20$  days and its eccentricity as near zero. The LBOI observations suggest that the star'scretion disk was axisymmetric in 2010, has an system inclination angle near  $45^\circ$ , and a larger radius than previously reported. In addition, the Be star began an "outburst" at the beginning of our campaign, made visible by a brightening and reddening of the disk during our campaign and beyond. Our analyses of the new high resolution spectra disclosed many attributes also found from spectra obtained in 2001 (*Chandra*) and 2004 (*XMM-Newton*). As well as a dominant hot ( $\approx 14$  keV) thermal component, the familiar attributes included: (i) a fluorescent feature of Fe K even stronger than observed at previous times; (ii) strong lines of N VII and Ne XI lines indicative of overabundances; and (iii) a subsolar Fe abundance from K-shell lines but a solar abundance from L-shell ions. We also found that two absorption columns are required to fit the continuum. While the first one maintained its historical average of  $1 \times 10^{21}$  cm $^{-2}$ , the second was very large and doubled to  $7.4 \times 10^{23}$  cm $^{-2}$  during our X-ray observations. Although we found no clear relation between this column density and orbital phase, it correlates well with the disk brightening and reddening both in the 2010 and earlier observations. Thus, the inference from this study is that much (perhaps all?) of the X-ray emission from this source originates behind matter ejected by  $\gamma$  Cas into our line of sight.

**Key words.** stars: individual:  $\gamma$  Cassiopeiae – stars: emission-line, Be – stars: activity – stars: winds, outflows – circumstellar matter

## 1. Introduction

Discovered in 1866 by Secchi from the emission in its H $\alpha$  spectral line,  $\gamma$  Cas became the first member of the now well known group of "classical Be" variables (Porter & Rivinius 2003). These stars are also known for their rapid rotation, continuum excess in the infrared, and by the presence of strong, blueshifted, and often variable, absorption components in their UV resonance lines. The latter were studied extensively in  $\gamma$  Cas and other Be stars at times intensively during the 1978–1996 operation of the International Ultraviolet Explorer (IUE). Fortunately, soon after of the termination of the operations of this

satellite, other techniques were being introduced to astronomy and have advanced the study of the Be stars and their ejected Keplerian disks. These developments include the operation of Long Baseline Optical Interferometry (LBOI) facilities, the development of automated photometric (robotic) telescopes, and an increasingly relevant contribution in spectroscopy by amateur astronomers with their own local facilities. The present study makes use of these elements.

Through the last decade astronomers have mounted a series of multi-wavelength campaigns on the prototype of the "classical" Be stars,  $\gamma$  Cas (HD 5394, type B0.5IVe). Even more

than most classical Be stars,  $\gamma$  Cas is variable over a number of wavelengths and timescales – see Harmanec (2002). The study of  $\gamma$  Cas developed renewed focus by the discovery that it emits X-rays with unusual properties and in particular by White et al.’s (1982) suggestion that these emissions arise from infall onto a degenerate companion. We now know that this star is in fact the primary in a nearly circular, 203-day binary system (Harmanec et al. 2001; Miroshnichenko et al. 2002). It may be important that its spectral lines are highly rotationally broadened ( $v \sin i \approx 400\text{--}441 \text{ km s}^{-1}$ ; Harmanec 2002; Freimat et al. 2005). With this broadening and a probable rotational period of 1.2158 days (Smith et al. 2006, “SHV”), this star is rotating at nearly its critical rate.

$\gamma$  Cas is also the prototype of a group that so far includes eight other Galactic “ $\gamma$  Cas X-ray analogs”. These include: HD 110432 (Smith & Balona 2006, “SB06”), SS 397, “Star 9” in NGC 6649 (USNO 0750-13549725; Motch et al. 2007), HD 161103 & SAO 49725 (Lopes de Oliveira et al. 2006; “L06”), HD 119682 (Rakowski et al. 2006; Safi-Harb et al. 2006), XGPS-36 (Motch et al. 2010), and HD 157832 (Lopes de Oliveira & Motch 2011). The X-ray properties of this group are not shared by the other classical Be stars.

In the years since the White et al. study, much effort has been devoted to characterizing the X-ray attributes of  $\gamma$  Cas itself because of its brightness. We know now that these properties include: (1) a rather high mean  $L_x/L \sim 10^{-6}$  (but at least 10 times lower than Be X-ray binaries); (2) a light curve variable on a number of timescales; and (3) a thermal spectrum consisting of 3–4 distinct plasma components. It is dominated by a hot component with temperature  $kT_{\text{hot}}$  of 12–14 keV and subject to absorption by two independent columns of cold (ambient) gas (Smith et al. 2004; Lopes de Oliveira 2010). It should also be remarked that the X-ray emission consists of an underlying “basal” component, which varies on a timescale of hours, punctuated by rapid flares that according to plasma cooling arguments alone must be produced in a high density environment (Smith et al. 1998a, “SRC”)<sup>1</sup>.

The X-ray light curve also exhibits variations on at least three timescales. Much of the behavior of the X-ray light curve of  $\gamma$  Cas is now well investigated by a series of relatively homogeneous RXTE studies (SRC, Smith & Robinson 1999; Robinson & Smith 2000; Robinson et al. (2006; “RSH”), and SHV). A rapid variability, first described in detail by Murakami et al. (1986), takes the form of ubiquitous flares on timescales of 2–3 min down to 4 s (the instrumental detection threshold). These flares are “mild,” only seldom having amplitudes of more than 2× above the background “basal” flux. The basal fluxes undergo undulations on timescales as short as 20 min but more typically a few hours. Thirdly, a long X-ray cycle of  $\sim 70$  day observed by RSH and SHV seem to be well correlated with long periods at optical wavelengths. The total range of these cycles in the optical range is about 50–91 days.

In this paper we seek to understand the X-ray emission generation in terms of its possible relationship to the general Be circumstellar environment, including both thecretion disk and its widely spaced binary companion. The impetus for this study was the different amounts of soft X-ray flux in earlier high-resolution spectra by *Chandra* and the *XMM-Newton* satellites (Smith et al. 2004; Lopes de Oliveira et al. 2010). The different soft X-ray flux levels are due to a density range (by a factor

of 40) in one of two absorption columns used in our models to fit the full *XMM-Newton* spectrum (the other column length solution was stable). We noticed that the 2001 *Chandra* observations were obtained during the binary phase of inferior conjunction, that is with the Be star passing through the foreground in its orbit. To see if the column density depends on binary phase, we requested four new exposures in 2010 for inferior conjunction phase and extending almost to quadrature. The question we posed was whether extra absorption would recur at this phase, e.g. due to absorption by matter near the Be star.

## 2. Description of the circumstellar matter

Many of the optical and X-ray variations from  $\gamma$  Cas are likely to be caused somehow by interactions of matter released by the star with its disk or with previous ejecta. Since the present study sheds new light on some these variations we should first review the status of the circumstellar (CS) structures.

*Geometry of the disk:* for several decades the emission from thecretion disk of  $\gamma$  Cas has varied irregularly, presumably because of discontinuous feeding of matter to itscretion disk (Doazan 1982; Doazan et al. 1987). The emission in the continuum is formed by free-free and bound-free process and in the hydrogen lines by recombination. Stee & Bittar (2001) found that the disk is optically thin at visible wavelengths but optically thick in the near infrared and in the  $H\alpha$  line out to greater disk radii. Their results indicated that the disk contributes  $\gtrsim 10\%$  to the total flux of the star-disk system in the Johnson V band but only 3–4% in B. Spectroscopic and interferometric arguments suggest that the disk and rotational axes coincide, and both techniques indicate that this angle, the inclination, has an intermediate value. For example, in their initial interferometric work in  $H\alpha$ , Mourard et al. (1989) determined a disk inclination angle of  $\sim 45^\circ$  from its measured ratio of the minor to major axis on the sky. Observations at this wavelength by Quirrenbach et al. (1997) and Tycner et al. (2006), with the MkIII and NPOI interferometers, respectively, as well as in the  $2.1 \mu\text{m}$  K' continuum band by Gies et al. (2007) have determined inclinations in a range  $i = 46\text{--}55^\circ$ .

LBOI studies have also determined the disk size of  $\gamma$  Cas. Tycner et al.  $H\alpha$  found a diameter of the major axis of 3.67 mas. This compared well with the Quirrenbach et al. (1997) measurement of 3.47 mas. In this paper we will adopt a uniform angular diameter for the Be star of 0.44 mas. Therefore, these measurements correspond to about  $8 R_*$ . In addition, most kinematic studies of Be disks have found that they have Keplerian rotation (e.g., Meilland et al. 2007b). Mourard et al. (1989) could show that the  $\gamma$  Cas disk rotates but were unable to specify its velocity-distance relation.

*Nonsecular variations imposed by the disk:* historically  $\gamma$  Cas has been among the  $\frac{1}{4}$  of classical Be stars for which the violet (“V”) and red (“R”) components of their Balmer emission lines exhibit cyclic variations with timescales of years (e.g., Hummel 2000). These cycles are believed to be caused by the precession of a 1-armed density structure from the excitation of non-axisymmetric disk modes (Okazaki 1991). They were first observed in Balmer lines of  $\gamma$  Cas in 1969 (Cowley et al. 1976). Continued observations in the 1980s–1990s disclosed a strong cycle with a length of 5–6 years. Berio et al. (1999) traced the precession of this arm over a few years by LBOI observations in  $H\alpha$ . Ritter Observatory spectra obtained by KSB show that the cycle was still present in 2000. Later observations by

<sup>1</sup> We define a flare as a sudden and short-lived increase in X-ray flux. This term does not necessarily connote a magnetic origin for them as on the Sun.

Rivinius (2007) indicate that the cycle weakened through 2003. By 2005 the  $V/R$  variations recorded by Ondrejov Observatory spectra were “very weak if present at all” (Nemravová 2011). Spectra obtained through the Be Star database (“BeSS”, Neiner et al. 2011) from 2009 to the present, including the epoch of our X-ray observations, show no variations either.

Typical of other classical Be stars observed at low or intermediate inclinations, the UV resonance “wind” lines in the  $\gamma$  Cas spectrum indicate the presence of a variable high velocity wind. Henrichs et al. (1983) found that optical depths in the wind lines can vary by a factor of up to 20 over time. The optical depths in the wind components increase by a mean factor of 2–3 times from  $V/R < 1$  to  $V/R > 1$  phases. Telting & Kaper (1994) advanced a picture in which the wind ablates disk matter, thereby focusing the wind and increasing column absorption at “blue” ( $V/R > 1$ ) phases. Beyond this modulation, changes in wind line strength can vary by up to a factor of five in a few weeks.

The cause of changes in the wind over these shorter timescales is a still unsolved mystery and is probably related to how Be stars change their local environment. In a distinctly different scenario from the Telting-Kaper picture, Brown et al. (2008) have suggested that a global magnetic field from the star focuses the wind towards the disk, thus producing a compressed and “magnetically torqued disk.” In such a picture one can imagine that time-dependent changes in the field geometry would focus the wind to varying degrees across our line of sight at different times, producing variations in the UV wind absorption components. This mechanism could not work for  $\gamma$  Cas globally because a dipolar field would produce unobserved strong periodic emission and absorption variations over the rotation cycle, as observed only in Bp stars. Still, it is conceivable that magnetic loops from chaotic surface fields could divert wind flows on smaller scales.

$H\alpha$  emission and optical brightening as well as reddening episodes in the optical records of  $\gamma$  Cas and other Be stars occur over timescales as short as a few weeks. In addition, Carciofi et al. (2012) have simulated a  $\sim 100$  day dissipation of the disk of the Be star 28 CMa with a viscous disk model and concluded the high Shakura-Sunyaev viscosity implied,  $\alpha = 1.0 \pm 0.2$ , requires that the mass injection rate into this disk exceeds the wind mass loss rate by about an order of magnitude. These considerations suggest that an unknown *deus ex machina* operates at irregular intervals that causes discrete ejection events (“outbursts”) in at least some Be stars. In Sect. 7 we will return to this topic. For now we will loosely use the term “wind” to indicate any type of ejection mechanism, although they may well involve more than radiative and centrifugal forces.

*Corotation and migrating subfeatures:* a number of observers have noted the existence of narrow absorptions called “migrating subfeatures” (msf) that run blue to red across optical and UV lines of the  $\gamma$  Cas spectrum. (Yang et al. 1988; Horaguchi et al. 1994; Smith 1995; Smith & Robinson 1999). In optical lines msf do not generally appear during every night of observation. When they do appear a new feature moves across a given point on the profile every 4–5 h and at an acceleration rate of  $+95 \text{ km s}^{-1} \text{ h}^{-1}$ . The msf have also been observed in spectral lines of the  $\gamma$  Cas analog HD 110432 (SB06) and the magnetically active, rapidly rotating K0 star AB Dor (Collier et al. 1989) and are ascribed to forced-corotation of dense clouds over the star’s surface by magnetic fields. Indeed, Donati et al. (1999) have confirmed the detection of a complex field topology on the surface of AB Dor, reinforcing the corotation interpretation.

The character of the spectroscopic msf makes it unlikely that they arise from nonradial pulsations (NRP). Recent photometric monitorings of Be stars have disclosed excited modes for which the periods tend to be clumped into noncoherent groups. For early-type Be stars they generally are excited with longer periods ( $\sim 0.5 \text{ day}^{-1}$ ) than the times between passages of successive msf absorptions<sup>2</sup>. The observed NRP modes are attributed mainly to rotational splittings of g-modes with  $|m| \approx 2$  (e.g., Walker et al. 2005; Dziembowski et al. 2007; Balona et al. 2011) or to inhomogeneities of orbiting disk matter (Balona 2009). Both their short lifetimes and their appearance as high frequency “wiggles” in the line profiles make the msf inconsistent with low- $|m|$  modes.

The interpretation of forced corotation of clouds was also advanced to explain dips in UV continuum light curves of  $\gamma$  Cas (Smith et al. 1998a, “SRH”). The span of these dips is too brief to be caused by advection of spots across the star’s surface. They can be explained, however, by the presence of translucent clouds corotating within a few tenths of the stellar radius of the surface. Also, the appearance of UV light curve dips correlates well with the increases in X-ray flux over several hours, according to a simultaneous X-ray/UV campaign described by SRC.

### 3. Origin of the X-ray emissions

The ultimate goal of our ongoing studies of this topic is to define the mechanism responsible for the unique emission of the hard and secondary soft X-ray emissions that set the  $\gamma$  Cas variables apart from the emissions of other high-mass stars. Most recent suggestions for this origin have centered around two competing ideas.

According to the first idea the hard X-rays result from the conversion of gravitational energy from accretion of the Be star’s disk onto the surface of a degenerate companion (white dwarf or neutron star). The primary rationale for this idea is the resounding success in explaining X-ray active Be stars in the Galaxy and Magellanic Clouds. Indeed, most of these X-ray sources are known to be binaries because of the detection of X-ray pulses due to a neutron star. In the case of the  $\gamma$  Cas stars no such pulses are known, and the direct detection of binarity through radial velocity variations has so far been confined to  $\gamma$  Cas itself. As already indicated, the near-circular orbit of this system hints that the secondary is not a neutron star. In this connection it may be significant that two members of the  $\gamma$  Cas group, “Star 9” of NGC 6649 and HD 119682 seem to be blue stragglers of clusters having ages of about 50 Myr and 40 Myr, respectively (Marco et al. 2007; Marco et al. 2009). Moreover, HD 110432 may be a member of NGC 4609 (age of 60 Myr; Feinstein & Marraco 1979), and if so would be a straggler. Thus, while unproven, it is conceivable that all  $\gamma$  Cas stars are blue stragglers. This circumstance could mean either that a current degenerate secondary star is the site of the X-ray emission or that it simply provides a mechanism to spin up the outer layers of the Be star to near criticality, thereby somehow triggering a mechanism for the production of the X-ray emissions.

Another argument for tying the X-ray emission to white dwarfs is the multi-thermal nature of the X-ray plasma observed in some cataclysmic variables, particularly the magnetic “polars” (e.g., Mukai et al. 2003). However, upon close inspection

<sup>2</sup> Exceptions to this statement are found in the spectral variations of  $\mu$ Cen and  $\delta$  Sco, which can exhibit modes with periods in this range in addition to others (Rivinius et al. 2003; Smith 1986). In these cases the appearance of broad sinuous NRP bumps on line profiles is very different than narrow msf depicted in the references we have cited.

there are also significant differences between the X-ray characteristics of these objects and  $\gamma$  Cas. These include in the former case a general lack of ubiquitous flaring confined to the hot X-ray regions and their exhibiting no differences in the Fe abundance determined from L and K shell ions (e.g., Itoh et al. 2006). In addition, even in their high states the hard components of polars have lower fluxes,  $L_x \sim 10^{30}\text{--}10^{32}$  erg s $^{-1}$  (e.g., Watson & King 1987) than  $\gamma$  Cas. If accreting white dwarfs are the source of the X-rays, it is likely that they would represent a new subclass of such objects.

A very different concept to explain the X-ray flux of  $\gamma$  Cas is called the “magnetic star-disk interaction” model and was proposed by RSH. These authors pointed to the X-ray flares noted above, the correlation of rapid variations of X-ray flux and UV and optical diagnostics associated with matter in the proximity of a Be star, some of which were noted above, as well as the correlation of the long X-ray and optical cycles. In this picture magnetic lines of force from active regions on the rapidly rotating Be star and its slower rotating disk occasionally get entangled. The result is that they stretch, sever, and upon reconnection fling high energy particles in various directions including toward the Be star. The impacts of these particles on random points on its surface heat photospheric plasma, and they become visible as “flares” – though not flares in the solar sense of releasing local magnetic energy. This matter expands to lower density regions above the flare site and continues to glow as “basal” emission. The observation of X-ray flux “lulls” over several epochs suggests that this does not happen perfectly continuously but instead can be subject to relaxation cycles.

The heart of the evidence for the Be star-disk magnetic interaction picture lies in observations of rapid correlations between X-ray flux and fluxes in other wavelength regimes and, secondarily, on inferences of magnetic activity on the star’s surface. The first well documented example of such a correlation was the report by Slettebak & Snow (1978) of an H $\alpha$  emission “flare” that occurred at the same time as short-lived occurrences of emissions in scanned components of the Mg II and Si IV lines by the *Copernicus* UV-scanning spectroscopic satellite. This could not be dismissed as a (double) instrumental “fluke” because *Copernicus*, using its coaligned X-ray telescope, also observed an X-ray during this time (Peters 1982). On another occasion, Smith (1995) observed a brief “emission flare” in the He I 6678 Å line, although no other wavelength regions were monitored.

To pursue this evidence SRC mounted a 21 h simultaneous campaign using the Rossi X-ray Timing Explorer (RXTE) and the *Hubble* Goddard High Resolution Spectrograph in 1996 March. They identified several correlations between X-ray and UV continuum flux as well as various spectral lines expected to be formed in the neighborhood of a B0.5 star (e.g., Smith & Robinson 2003). These variations are the strongest single set of arguments that the X-rays are excited near the surface of the Be star.

The correct explanation for the production of the hard X-rays will have interesting ramifications for our understanding evolutionary and possibly the angular momentum history of the X-ray emitting star. The elucidation of this true mechanism will require the pulling together of diverse properties of the Be star, its binary orbit, and circumstellar matter from observations at several wavelength regimes over as contemporaneous a time interval as possible. The following describes a comprehensive effort to this end.

## 4. Observations

We first outline the observational techniques used in this paper. We begin by summarizing the LBOI results and discussing results from automated photometry and H $\alpha$  line spectroscopy.

### 4.1. The CHARA long baseline optical interferometer

Our LBOI observations were conducted in the infrared using Georgia State University’s Center for High Angular Resolution Astronomy (CHARA) array facility on Mt. Wilson. CHARA is an interferometric array of six 1-m telescopes configured in a Y-shaped pattern with baselines of up to 330 m for maximum spatial resolution. Our observations utilized two new-generation instruments for imaging of  $\gamma$  Cas’s decretion disk: the Michigan Infrared Combiner (MIRC) in the *H*-band (1.64  $\mu$ m) and the Visible spEctroGraph and polArimeter (VEGA), which became operational in 2009 (Mourard et al. 2009). VEGA observations were conducted in H $\alpha$  and also near this line in  $\sim$ 200 Å regions centered at 6460 Å, 6690 Å, and 6728 Å. In the first case the results from the three wavelength settings were averaged together and we call the result the “R”-band measures. The H $\alpha$  line fluxes were determined by stepping in 3 Å steps across the 6550–6575 Å region. The observations were executed in order to describe the geometry of the Be disk. The VEGA kinematical program was conducted to test the disk rotation-radius relation. These observations are summarized in the following and are detailed in Stee & Mourard (2012, “Paper II”).

The MIRC instrument was used in a 4-telescope arrangement, resulting in the simultaneous measurement of 6 visibilities, 4 closure phases and 4 triple amplitudes. These observations used a broadband *H* filter along with a prism to disperse the light into 8 spectral channels ( $R \sim 45$ ). This light is refocused to produce interference fringes received by a “PICNIC” camera designed to maximize rapid data readout and minimize fringe decoherence due to atmospheric seeing. Further details on this electronic and readout system may be found in Monnier et al. (2004, 2008), Pedretti et al. (2009), and Che et al. (2010). The maximum angular resolution  $\frac{\lambda}{2B}$  in the *H* band using the MIRC at CHARA is 0.4 ms, or coincidentally about the expected angular size of  $\gamma$  Cas, the Be star. The observations for this study were carried out on 2010 Aug. 5, Aug. 8, Sept. 24, and Nov. 4–5. This range of dates includes the range of the *XMM-Newton* OBS 3 and 4 referred to below and the next two months. These observations were followed almost immediately by VEGA observations. The MIRC baselines ranged from 34 m (S1S2) to the maximum 330 m (S1E1).

The VEGA instrument is different from MIRC in working with visible wavelength (4500–8500 Å) light at “low, medium, or high” dispersions (1700, 5000, 30 000) but enables the combining of light from up to four CHARA telescopes and measurements of visibility modulus, phases, and phase closures as a function of baseline and wavelength. Its angular resolution is 0.3 milliarcsec in the visible. The addition of a Wollaston prism allows the study of polarization across velocity dispersed systems, such as the circumstellar disk of  $\gamma$  Cas. The performance of the basic instrument is summarized by Mourard et al. (2011).

Begun in 2008, the VEGA observations of  $\gamma$  Cas are summarized in this paper and noted in Paper II. As noted in the latter, half of them were contemporaneous with the *XMM-Newton* observations, and most of these measurements were made over a variety of configurations. A limitation of our VEGA dataset is that the observations were clustered near the same minimum baseline ( $\sim$ 30 m) in the south (S1S2) alignment. The W1W2 baseline was

more than adequate to resolve the disk in the east-west direction on the sky. However, this mismatch in configurations limited our ability to verify the presence of features in the south-north direction on the disk, even though departures from disk axisymmetry have been observed with earlier generations of equipment (e.g., Berio et al. 1999). Also, we were unable to get a complete set of phase closures at multiple times. This means that we could not determine time-dependent differences during the 2008–2010 interval.

#### 4.2. The Automated Photometric Telescope observations

Our optical continuum observations of  $\gamma$  Cas were made in the standard Johnson  $V$  and  $B$  band filters on every available photometric night (sometimes several times per night) using the 0.4 m T3 Automated Photometric Telescope (APT) located at Fairborn Observatory in the Patagonia mountains in southern Arizona. Our monitoring of this star began in 1997 September and has continued every year since, with an observing season lasting from September into February and restarting again briefly in mid-June, weather conditions permitting. We lose about two months of the  $\gamma$  Cas observing season due to monsoon rains.

Full details concerning our APT observational program on  $\gamma$  Cas can be found in RSH and SHV. Briefly, the observations are made by cycling the automated telescope between the program star and the nearby stars HR 6210 (F6 V) and HD 5395 (G8 IIIb), which are used as comparison and check stars, respectively. The APT executes each observing sequence as follows: K, S, C, V, C, V, C, S, K, where K, C, and V, are the check, comparison, and program stars, respectively, and S is a sky observation. Each complete sequence is termed a “group observation” or simply a group. All integration times were 10 s, and all measurements were made through a 3.8 mag neutral density filter to attenuate the counts and avoid large deadtime corrections. The program star is thus bracketed by the comparison star on both sides three times during each group measurement at a cadence of 8 min. Group mean  $V - C$  and  $K - C$  differential magnitudes are computed and standardized with nightly extinction and yearly mean transformation coefficients determined from nightly observations of a network of standard stars. Typical rms errors for a single observation, as measured from pairs of constant stars, are  $\pm 0.0030$ – $0.0035$  mag. The rms scatter of the seasonal mean  $K - C$  differential magnitudes, inferred from differences of the 40th and 60th percentile of fluxes during a season (a reliable internal metric) is  $\sim \pm 0.003$  mag., indicating good long-term stability. By comparison, the corresponding figure during the 2010 season was twice as large,  $\pm 0.007$  mag. This was also near the value of the formal rms. These larger values are largely due to the quasi-secular brightening during this time.

#### 4.3. Optical wavelength spectra of $\gamma$ Cas

To support this program we made use of 306 echelle spectra of  $\gamma$  Cas taken in a long-term monitoring program with the spectrograph fiber-fed from the Cassegrain focus of the 1.06-m telescope at Ritter Observatory (administered by the University of Toledo) in 2009 December and the second half of 2010. The spectra were obtained using a new Spectral Instruments, Series #600 camera configured in an echelle format. This resulted in a resolution of 27 000. We used three echelle orders to extract the  $H\alpha$  spectrum and background, extending over the range 6285–6834 Å. Exposures lasting a few minutes gave spectra with a signal to noise ratio of  $\approx 100$ .

Our dataset includes  $H\alpha$  spectra by Pollmann who used a cooled CCD camera with  $9 \times 9 \mu\text{m}$  pixels attached to the Cassegrain focus of his 35 cm Schmidt telescope in Leverkusen. A dispersion of  $22.2 \text{ \AA mm}^{-1}$  made for a spectral resolution of 16 400 over the range 6520–6700 Å. In Hamburg Bücke used a 20 cm Dobson Telescope fiber coupled to a spectrograph contain a cooled CCD camera with  $18 \times 200 \mu\text{m}$  pixels. This system provides a dispersion of  $0.56 \text{ \AA pixel}^{-1}$  and a spectral resolution of 3400 extending over a range 5900–6700 Å. These instruments have been used in stable configurations for several years.

#### 4.4. XMM-Newton observations

We conducted four *XMM-Newton* observations under the auspices of Guest Investigator cycle A09. These were carried out on 2010 July 7 (ObsID 0651670201; referred to here as OBS1), July 24 (0651670301; OBS2), August 2 (0651670401; OBS3), and August 24 (0651670501; OBS4), beginning on MJD dates 55 384.30, 55 401.15, 55 410.77, and 55 428.09, respectively; *XMM-Newton* prefers the MJD time system. The observations OBS1 to OBS4 had total effective exposure times of 17.5, 15.7, 17.5 and 22.4 ks for the pn detector, respectively, 0.2 ks longer times for the MOS1 and MOS2 cameras, and 0.4 ks for the RGS cameras. High energy-sensitive data were taken through the thick filter of the European Photon Imaging Camera (EPIC) camera operating in small window mode. To avoid high noise contributions from soft energies, our timing analyses were restricted to EPIC data in the 0.8–10 keV energy band. Our spectral analysis made use of the complementary information of the medium resolution EPIC spectra between 0.2 and 12 keV and high resolution RGS spectra from 0.3 and 2 keV. Data reduction, spectral analysis and part of the timing analysis were carried out using SAS v10.0.0, XSPEC, and Xronos package, respectively. See <http://heasarc.nasa.gov/xanadu/spec/> for a description of these packages.

Altogether we used five *XMM-Newton* cameras in our observations. Of these the EPIC detectors (pn, MOS1, and MOS2) were especially important for the evaluation of the hot plasma component. The RGS1 and RGS2 cameras were more important for assessing the warm and cool plasma components defined below, and exclusively in determining spectral line attributes for lines above 10 Å. The optical monitor was turned off during our observation.

### 5. Results of optical investigations

#### 5.1. Fitting of CHARA visibilities of the $\gamma$ Cas system

In this section we summarize the interferometric results obtained in our collaborative program.

We were able to resolve the disk diameter in both  $H$ -band and  $R$ -band using LITpro model programs (for details see [http://www.jmmc.fr/litpro\\_page.htm](http://www.jmmc.fr/litpro_page.htm)). We fit the MIRC data with two three-component models, that is with a uniform brightness star disk, a Be disk and a uniform “background” comprising 12–14% of the total flux. Such a component is not the norm for Be-disk descriptions. Physically it could be due to the presence of previously ejected matter from the star that is now extended beyond the disk. In the first model the Be disk is assumed to have a Gaussian profile with distance from the center of the star. In the second model the disk model is an elliptical ring of equal surface brightness, with a brightness cutoff at the inner and outer edges. The motivation for the ring model was

**Table 1.** Relevant star and Be disk fitting parameters from LBOI.

MIRC DATA: IR <i>H</i> -band	Gaussian disk model	Ring disk model
Parameter		
Star diameter (mas)	0.44 ± 0.03	0.44 ± 0.03
Inclination angle ( $i$ ) (thin disk or ring)	42 ± 1°	44 ± 1°
Minor disk axis (mas) ( <i>Linear, in <math>2R_{\odot}</math></i> )	0.62 ± 0.08 1.4	... ...
Major disk axis (mas) ( <i>Linear, in <math>2R_{\odot}</math></i> )	0.82 ± 0.08 1.86	... ...
Minor ring inner diam. (mas) (major axis)	n/a	0.60 ± 0.33
Outer ring diameter (mas) along the major axis	n/a	0.85 ± 0.45
Flattening ratio	1.33 ± 0.08	1.39 ± 0.08
Position Angle (E from N in degrees)	12 ± 9	12 ± 9
Star flux (%)	35 ± 1	45 ± 6
Disk/ring flux (%)	53 ± 2	41 ± 6
Background flux (%)	12 ± 1	14 ± 1
$\chi^2$	3.96	3.95
<hr/>		
VEGA: near-H $\alpha$ “R”-band	Gaussian disk model	Ring disk model
Parameter		
Star diameter (mas)	0.44±0.03	(no fit)
Inclination angle ( $i$ ) (thin disk)	42 ± 3°	n/a
Minor disk axis (mas)	0.56 ± 0.05	n/a
Major disk axis (mas) <i>Major axis (in <math>2R_{\odot}</math>)</i>	0.76 ± 0.05 1.72	n/a
Flattening ratio	1.36 ± 0.08	n/a
Position angle (E from N in degrees)	19 ± 5	n/a
Star flux (%)	55 ± 2	n/a
Disk flux (%)	45 ± 2	n/a
$\chi^2$	1.95	large

to determine whether there is a star-disk gap that might arise from solid body rotation of clouds within the radius. However, we were unable to get a satisfactory fit to the VEGA data using the ring model. Table 1 shows the results. The angular values in milliarcsec here are converted to linear dimensions and represented in italics, assuming the distance and value of  $R_*$  given in Sect. 1.

Using these models with the MIRC data, we resolved a flattened circumstellar disk with elongation ratios of  $0.82/0.62 = 1.33$  (Gaussian) and  $0.85/0.60 = 1.39$  (ring). The VEGA *R*-band data led to an elongation of  $0.76/0.56 = 1.36$ . The MIRC values give an inclination  $i \approx 42^\circ$  and  $44^\circ$ , respectively. The VEGA *R*-band results are essentially the same,  $i \approx 42^\circ \pm 3^\circ$ . Likewise, the position angle derived from the VEGA is  $19^\circ \pm 5^\circ$  and thus consistent with the MIRC value. For the MIRC solution the ring radius extends from  $1.4 R_*$  to  $2.0 R_*$ , but the error bars are large.

As Table 1 shows, we were unable to get a satisfactory solution for the VEGA *R*-band data with a ring model.

We also used the VEGA system to measure fluxes in the H $\alpha$  line both spatially and kinematically. In this analysis we adopted the major axis and inclination angle from the *R* band analysis outlined above. Our best fitting major axis parameter in H $\alpha$  flux is  $4.4 \pm 0.4$  mas. The position angle was measured as  $20 \pm 15^\circ$ . Assuming the previous parameters, we find a Be disk radius of  $10 \pm 1 R_*$ . We point out that at  $10 R_*$  the VEGA disk radius is nearly half the Be star’s Roche lobe radius (of some  $21.4 R_*$ ; Gies et al. 2007). We find from Okazaki & Negueruela (2001) that the most likely 3:1 resonance truncation radius of the disk due to the companion in a circular orbit is about 0.4 of the orbital separation, or  $\approx \frac{3}{4}$  of the Roche lobe radius. Our VEGA radius does not yet reach this extent, but one may hope more sensitive future observations, particularly in the far-IR, that could test for the presence of a truncation edge.

Our kinematic observations for H $\alpha$  were designed to determine the exponent value  $\beta$  in the velocity distance relation in the disk,  $V_\phi = (r/R_*)^\beta$ . We obtained a value of  $\beta = 0.5 \pm 0.1$ , or exactly the Keplerian rotation result. Solid body rotation, for

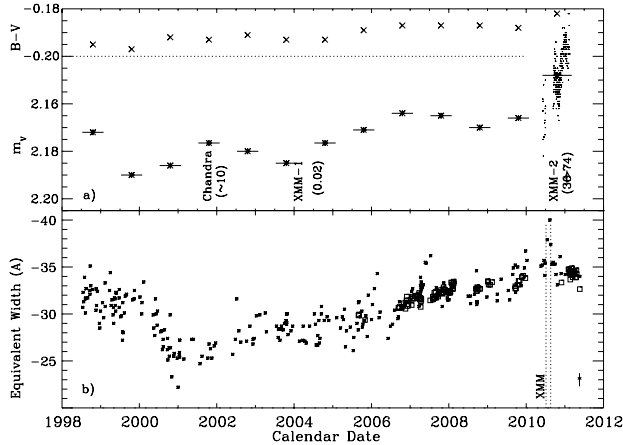


**Fig. 1.** a) APT  $V$  ( $m_V$ ) magnitudes and ( $B - V$ ) color of  $\gamma$  Cas over the 1998–2010 seasons of coverage; annual averages are shown. Error bars on these magnitudes (marked as \* and X, respectively) are much smaller than the symbols, as each point represents a few hundred individual observations. Horizontal bars denote the coverage in time for each season's average. Small points indicate each  $m_V$  value measured in the 2010–2011 season. Annotations at the bottom give the column densities  $n_{H_b}$  in units of  $10^{22} \text{ cm}^{-2}$  responsible for the attenuations of soft X-rays in high dispersion X-ray observations of 2001, 2004, and 2010. b) the  $H\alpha$  emission equivalent widths ( $EW$ ) in Ångstroms obtained by Pollmann and Bücke (star and square symbols, respectively) over the same time as panel a)). A displacement of  $-1.0 \text{ \AA}$  was required to bring the the mean Bücke  $EW$  to the Pollmann mean. The vertical dotted lines correspond to times of the first and last *XMM-Newton* observations in 2010. Note the rapid  $H\alpha$  emission increase from 2002 on, and also a similar spike in 2007 as observed in 2010. Both events coincide with  $m_V$  brightenings when panel a is plotted in high time resolution.

which  $\beta = -1$ , is therefore (unsurprisingly) ruled out for the whole disk. The confluence of Keplerian rotation with corotating clouds over the star's surface suggests a complicated geometry for the CS matter.

## 5.2. Optical photometry and spectroscopy

### 5.2.1. Combining the APT light curve and $H\alpha$ measures

Figure 1a plots the seasonal mean Johnson  $V$  magnitudes and mean ( $B - V$ ) color indices from the T3 APT for the 13 observing seasons from 1998–2010.<sup>3</sup>

Notice a series of long-term erratic undulations over timescales of 2–3 years. This variability pattern probably results from structural changes in the disk, but the details of this are unclear. We can shed some light on this by coplotting the  $H\alpha$  measures in Fig. 1b. Although the light curve shows highly statistical fluctuations from year to year, over the entire timespan the slopes of both  $H\alpha$  equivalent width and  $V$ -band light curves are positive – that is, the activity as defined by  $H\alpha$  emission, magnitude brightening, and  $B - V$  color have increased more or less together. Thus the  $H\alpha$  emission from the CS disk correlates with optical continuum brightening.

<sup>3</sup> We define the “1998” season as the interval from 1998 June–1999 February. Note that we omit the 1997 observing season because a neutral-density filter change in 1998 resulted in new magnitude zero-points from 1998 onwards. Analysis of the variability in 1997 was published by SHV. Errors in the seasonal means are very small and are due mainly to incomplete averaging of the long cycles and/or slopes in the magnitude.

**Table 2.** Ritter & Dobson/RB radial velocities (stub).

RHJD	$\Delta RV$	Error	O-C	Phase	Source
51 571.510	1.63	0.92	-2.16	0.00	Ritter
51 586.504	3.04	1.32	-0.30	0.08	Ritter
51 608.527	0.38	1.31	-1.09	0.19	Ritter
51 609.516	-0.22	1.69	-1.59	0.19	Ritter
51 777.805	3.80	5.81	0.04	0.02	Ritter
51 794.820	2.87	1.64	-0.17	0.10	Ritter
51 800.800	0.31	1.19	-2.26	0.13	Ritter

Inspection of the two curves in Fig. 1 shows that second order deviations in their behaviors exist. These include a delay in the decrease in the  $H\alpha$  emission index over the reduced heliocentric Julian date (RHJD) range 51 040–51 080, absences of rises in the index at RHJD 52 000–52 400 and at 54 000–54 200, and absence of a rapid upturn at the end of the data sequence. Such deviations can arise because of differences in the optical thickness in the  $V$ -band continuum and the  $H\alpha$  line core. The optical depth in the  $H\alpha$  line is many times more optically thick than the  $V$ -band continuum (see e.g., Carciofi 2011) and therefore the point at which  $\tau_{disk} = 1$  lies further from the star. Consequently, the  $H\alpha$  emphasizes disk changes at greater radius than the  $V$  continuum does.

### 5.2.2. A revised radial velocity solution for the binary orbit

We measured the radial velocities for the  $H\alpha$  spectra from Ritter Observatory by computing bisectors of the emission line components. For this purpose we used the method of Shafter et al. (1986), which has special application to measurements of shifts of asymmetric line profiles. The bisector position is determined by creating a function composed of a negative-valued Gaussian (offset by  $\Delta V = -300 \text{ km s}^{-1}$ ) and a positive-valued Gaussian (offset by  $\Delta V = +300 \text{ km s}^{-1}$ ); both Gaussians have a width  $FWHM = 85 \text{ km s}^{-1}$ . This function is then cross-correlated with the observed emission lines (whose baseline is reset to zero), and the zero-crossing of the resulting cross-correlation function yields the bisector position. We measured 198 velocities from Ritter Observatory that span from 2000 January 28 to 2010 November 11. Also, one of us (RB) obtained 103 new measurements over the interval 2006 September 20 through 2011 April 22 from the Hamburg Dobson Telescope system. These were measured by fitting a Gaussian function to the profile. Finally, we combined the Ritter and RB velocities. The weights of the Ritter data were determined from the mean continuum signal-to-noise ratio in the spectra. Because the RB spectra were measured from lower resolution spectra, we assigned them a higher velocity error of  $\pm 3.16 \text{ km s}^{-1}$ . The RB origin can be found from this assignment in Table 2. To bring the Ritter and DB velocities to a common mean of zero, we added  $5.73 \text{ km s}^{-1}$  and  $9.95 \text{ km s}^{-1}$  to the Ritter and RB velocities, respectively. The results are shown in Table 2 as a stub (dates in Reduced Heliocentric Julian Dates). The full data list of 301 radial velocities is given in the electronic version of this paper. Column 3 is the measurement error in  $\text{km s}^{-1}$ ; Col. 4 is the “O–C” (Observed minus Computed) differences; Col. 5 the orbital binary phase, and Col. 6 is the RV source (Ritter or RB).

In order to construct a new orbital solution, we first examined these new data and found evidence for long-term trends introduced by including pre-2000 radial velocities. We did not include these early data because the methods for pre-whitening

**Table 3.** Orbital solution for  $\gamma$  Cas.

Parameter	Units	1	2 (adopted)
$K$	(km s $^{-1}$ )	$3.80 \pm 0.08$	$3.79 \pm 0.08$
$e$		$0.03 \pm 0.02$	...
$\omega$	(degrees)	$198 \pm 29$	...
$T$	(RHJD)	$55\,549.48 \pm 16.32$	...
$T_{\text{RVmax}}$	(RHJD)	$55\,436.47 \pm 0.64$	$55\,438.1045 \pm 1.35$
$P$	(days)	$203.590 \pm 0.21$	$203.555 \pm 0.21$
$f(M)$	( $M_\odot$ )	$(0.116 \pm 0.008) \times 10^{-2}$	$(0.115 \pm 0.007) \times 10^{-2}$
$a_1 \sin i$	( $R_\odot$ )	$15.28 \pm 0.33$	$15.23 \pm 0.33$
rms	(km s $^{-1}$ )	1.03	1.03

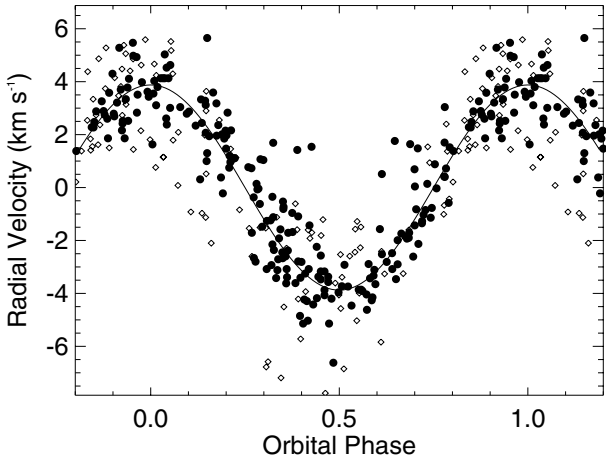


**Fig. 2.** The adopted radial velocity solution from our Orbit 2 model (see Table 3). Solid dots and open triangles are measures obtained from Ritter Observatory and RB's Hamburg system, respectively. The weights to the sinusoidal solution are lower for the open symbols. Table 2 gives errors for all observations.

could introduce new artifacts in the analysis of the orbital elements. We made an error-weighted fit to the velocities to solve for orbital elements using the program of Morbey & Brosterhus (1974). We solved for the orbit by allowing the eccentricity  $e$  as well as other orbital parameters to float freely. This solution is represented as Orbit 1 in Table 3. Discovering that this eccentricity is at most no more than marginally significant (e.g., from testing the probability index  $p_1$  suggested by Lucy 2005), we ultimately adopted the circular solution with the same period. This is given Orbit 2 in our table. We depict the folded data to the Orbit 2 solution as a 203.555 day sinusoid in Fig. 2. Phase zero for Orbit 2 is referred to the maximum velocity. For Orbit 1 we adopt the time of periastron passage.

Our derived orbital parameters for  $\gamma$  Cas differ slightly from the discovery analyses of Harmanec et al. (2001) and Miroshnichenko et al. (2002). The first study found  $e = 0.26$  and  $P_{\text{orb}} = 203.59$  days, and the second  $e = 0.0$  and  $P_{\text{orb}} = 205.50$  days. Essentially, our new period solution agrees with Harmanec et al. but our eccentricity value agrees with Miroshnichenko et al. Shortly before submission of our results for publication, we received a preprint from Nemravová and collaborators describing a radial velocity study covering nearly 17 years of the star's velocity history (Nemravová et al. 2012). Their results and ephemeris are substantially the same as our own. Their estimate of the period,  $203.52 \pm 0.08$  days, is well within the formal errors of our two analyses. The same comment

applies to the errors in  $T_0$  and phases. Therefore, we believe a synthesis of our works leads to a definitive orbital parameters.

From the parameters in Table 3, if we assume a mass of  $15 M_\odot$  for the primary and an inclination of  $45^\circ$  and assume that the binary orbit and Be disks are coplanar, we may adopt the mass function of  $1.15 \times 10^{-3} M_\odot$  to find a most probable secondary mass of  $0.8 M_\odot$ . Assuming reasonable errors for the primary mass ( $\pm 1 M_\odot$ ), an inclination of  $45^\circ$  ( $\pm 6^\circ$ ), and  $K_1$  ( $\pm 0.1 \text{ km s}^{-1}$ ), we estimate a generous error of  $\pm 0.4 M_\odot$  for the secondary. This estimate supports the possibility that the secondary could be a late type dwarf, white dwarf, or a sdO star, but probably not a neutron star. This justifies the omission of this star from adding an additional optical stellar component in our LBOI models.

If we adopt the Orbit 2 determination in Table 3, our orbital phases corresponding to the *XMM-Newton* observations discussed below are  $\phi_{\text{orb}} = 0.74, 0.82, 0.87$ , and  $0.96$  (where again  $\phi_{\text{orb}} = 0.0$  is defined relative to the epoch of maximum RV). The Nemravová et al. RV orbital ephemeris gives phases for these observations of  $0.73, 0.81, 0.86$ , and  $0.95$ , i.e., within 0.01 of our values. As for our solution, Nemravová preferred a circular solution to even small values of the eccentricity. In considering the relative weighting of these two RV studies, we can take the errors at face value and double weight the Nemravová et al. solution relative to our own. This gives a period of  $203.53 \pm 0.10$  days.

To summarize, the first of the 2010 *XMM-Newton* observations was conducted just as the Be star was in inferior conjunction with respect to its secondary, similar to the phase of the 2001 *Chandra* observation. The last of the four observations coincided with the Be star essentially at quadrature phase. With this ephemeris one finds that the phase of the 2004 *XMM-Newton* observation was 0.27.

## 6. Analysis of *XMM-Newton* observations

Herein we discuss four high-quality *XMM-Newton* exposures of  $\gamma$  Cas in 2010, dubbed OBS1-4 above. The star was previously observed in high resolution on two occasions: in August, 2001, by the High Transmission Energy Grating of *Chandra* (HEG/MEG) and in February, 2004, by XMM (RGS) (Smith et al. 2004; Lopes de Oliveira et al. 2010). We can combine the photometric and spectroscopic results to get a sense of epochal differences of the conditions responsible for X-ray emission.

### 6.1. *XMM-Newton* light curve variations

We began the analysis by extracting light curves binned to 20 s for hard- (4.5–10 keV), soft- (0.3–1 keV), and the total flux over 0.3–10 keV for each of the four observations. The median

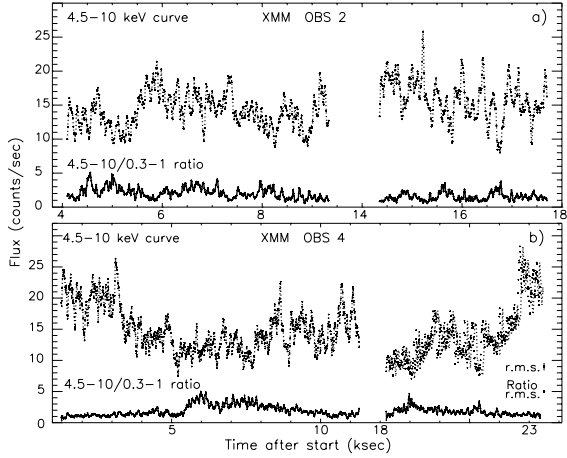


**Fig. 3.** Two stretches of *XMM-Newton* light curves and color ratios for OBS2 and OBS4. The light curves are binned to 20 s and smoothed over two points. The rms errors are indicated taken from point to point fluctuations, with the same smoothing. The color ratios have been scaled by 5 $\times$  for visual clarity. Occasional flare aggregates are obvious in the light curves. The lower plots in the two panels disclose the color variations only over timescales of  $\gtrsim$ 0.6 ks.

fluxes of three of the light curves extracted from the *pn* detector (0.3–10 keV) are about the same, about 25.0 counts s $^{-1}$ . The mean flux of the third observation at MJD 55 410 is 47% higher than the mean of the other three, among which the difference is only  $\pm$ 7%. Given the assumed distance of 168 pc, this means that the  $L_x$ 's for the observations lie in the range  $8\text{--}13 \times 10^{32}$  erg s $^{-1}$ . This range is somewhat higher than the range  $3\text{--}9 \times 10^{32}$  erg s $^{-1}$  from RSH using the RXTE several years earlier.

The light curves and hard/soft color ratios for OBS2 and OBS4 are shown as examples of all four observations in Fig. 3. Note that the light curve exhibits the usual pattern of almost uninterrupted flaring.

As with previous light curve studies, we find also that soft- and hard-energy light curves constructed track one another very well, giving only occasional significant departures from a mean color ratio. There is in general a remarkable absence of color hardening during strong flares or brief near cessations in emission. In fact, most of the largest color fluctuations occur when no strong flux excursions (flares or flux lulls) occur. Yet we do find occasional departures from a uniform color. For example, we found a few sinuous variations in color curves in each of the four observations. An example is depicted for stretches for OBS2 and OBS4 – see Fig. 3. In OBS4 sudden hardenings occur over 0.5–1 ks and are followed by a slow return to the mean color over a few ks. Sometimes hard flux changes are followed by soft fluxes, but not quite to the same degree (e.g., the “decays” in Fig. 3b). At other times they occur when the hard component is nearly constant or undergoes apparently stochastic fluctuations (Fig. 3a). In almost all these cases the soft component changes more slowly, on timescales of 100–1000 s, in the fashion shown in these plots.

The power spectrum, summed over our four observations, is exhibited in Fig. 4. It shows the beginning of a logarithmic slope just exceeding  $-1$  for  $\geq$ 30 s flare-like excursions. At about 0.005 Hz it breaks to a shallower slope. This is consistent with the break at  $1\text{--}3 \times 10^{-3}$  Hz reported by Robinson & Smith (2000). We characterize the occasional variations on timescales longer than flares as “undulations”. SRH and RS have shown that these features are most likely due to the passage of translucent clouds forced into corotation over the Be star. They suggested that these

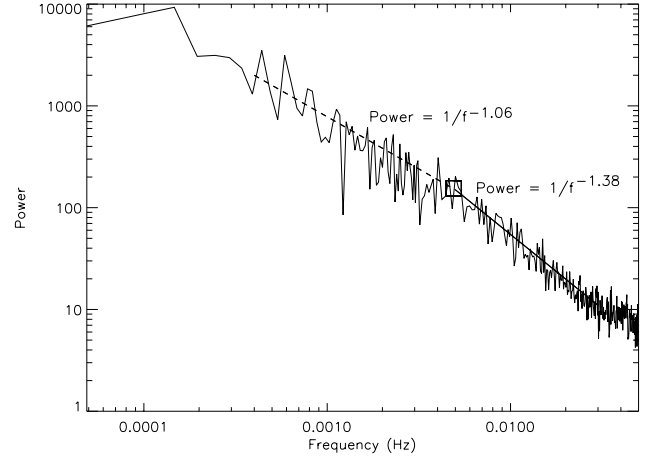


**Fig. 4.** Sum of power spectra of our four /XMM/EPIC pn observations over 0.8–10 keV of  $\gamma$  Cas. The binning in time over 10 s prevents the spectrum from being followed out to its white noise component. Regression lines are drawn with slopes noted through two frequency ranges. A break in the slopes is noted by a square symbol at a frequency of 0.005 Hz.

are responsible for the continued rise in power above the break in the slope of the power spectrum. Looking to shorter timescales, we performed an autocorrelation analysis on the integrated light curves as well as light curves separated into binned soft and hard fluxes. However, we found that none of them exhibited quasi-periods. Also, we found that to a precision of 1–2 s we could find no evidence of time delays between the hard and soft flux time series.

## 6.2. Spectral analysis: primary parameters

*Description of XMM-Newton spectra:* The 2010 *XMM-Newton* spectra appear similar to those obtained by *Chandra* in 2001 (Smith et al. 2004) and the *XMM-Newton* in 2004 (Lopes de Oliveira et al. 2010, “L10”). The spectrum is “hard,” i.e., most continuum flux is emitted at energies of a few Ångstroms or lower. The long wavelength continuum is attenuated much like the *Chandra* spectrum and in contrast to the unattenuated 2004 *XMM-Newton* spectrum. The visible emission lines in the long wavelengths of the RGS spectral detectors are the Ly  $\alpha$ -like lines of even-nucleons Mg XII, Ne X, and O VIII, and the *i* and *f* components of the so-called *fir* complex of the ground-level helium-like ions Ne IX and O VII. The Ly $\alpha$ -like emission lines of the Fe K shell ions Fe XXVI and Fe XXV are likewise visible in the short wavelength spectra of the EPIC/MOS and *pn* detectors. An additional emission feature at  $\approx$ 1.94 Å arises from atoms of less excited Fe ions, the so-called Fe K fluorescence feature. Similarly, in three of the four RGS camera spectra we found faint corresponding features due to Si K ion fluorescence, as previously reported by Smith et al. (2004, “S04”). In addition, the RGS spectra exhibit a number of emission lines of Fe XVII and Fe XVIII (Fe L shell) ions. The quantitative analyses of our line strengths and broadenings were performed independently for spectra recorded by the *pn* and MOS detectors at short wavelengths and for the RGS1 and RGS2 detectors at long wavelengths because the instrumental responses and calibrations for these cameras are different. Following *XMM-Newton* mission recommendations we have performed quantitative analyses with XSPEC using all individual EPIC and RGS spectra simultaneously.

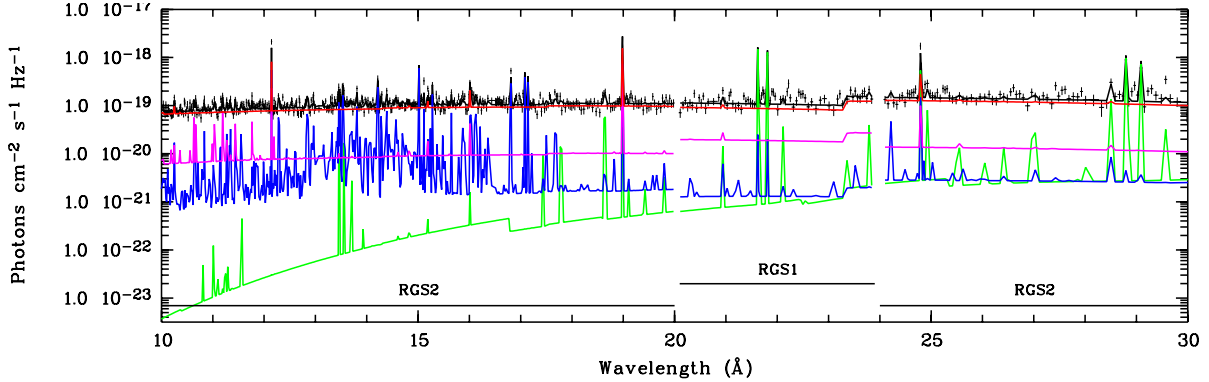


**Fig. 5.** Color-coded “unfolded” model spectra in the range 10–30 Å computed for RGS1 and RGS2 for the fitted model of OBS3. The green, blue, purple, and red denote the normalized emission spectra of plasma components  $kT_1$ ,  $kT_2$ ,  $kT_3$ , and  $kT_4$ , each with the single values given in Table 4. The black line is the observed spectrum. The model from the RGS2 detector was used for all wavelengths except for the 20–24 Å gap, and for this gap the RGS1 model was used. This accounts for small discontinuities in the emissions at these wavelengths for the  $kT_2$  and  $kT_3$  plasma components. The  $kT_3$  and  $kT_4$  emission are almost as well described by a broad DEM centered at a high energy.

*Using XSPEC to determine multi-temperature models.* We used the same suite of *ftools* and XANADU/XSPEC tools to fit our *XMM-Newton* spectra that L10 used – mainly *mekal*, *vmekal*, and *cevmkl*. We also used the XSPEC model *bvapec* to determine measures of line widths and certain elemental abundances. All of these models assume one or more optically thin and thermal plasma components that are also in coronal ionization equilibrium. The *mekal* model families are then parameterized by a series of mono-thermal plasma components and their normalizations (proportional to emission measures, “EMs”). The normalizations in the various cameras were independent of one another and all were kept free during the fit. This procedure was adopted to assure that each individual normalization takes into account the difference in calibration of the cameras. Ultimately we adopted the mean value of the normalization of each camera and for each plasma component to compute an emission measure from its recorded spectrum. However, in doing so we neglected the weak and uncertain high energy response of the RGS cameras, which can otherwise bias the result. A Gaussian emission feature was added to the model to parameterize the visible Fe fluorescence line at 1.9 Å. We also included necessary multiplicative photoelectric absorption terms, parameterized by the term “ $n_{H_i}$ ,” which correspond to the equivalent hydrogen columns. These parameters are combined in a simultaneous solution to fit the continuum and emission lines. In general, a number of iterations are required for convergence. We experimented with different starting temperatures to avoid converging to false solutions.

As in L10 we tried to fit the  $\gamma$  Cas *XMM-Newton* spectrum with a continuous differential emission measure (DEM) defined as a cooling flow model (e.g., *cevmkl*)<sup>4</sup>. While this is sometimes considered the preferred X-ray emission description for accreting white dwarfs, it does not work for our spectra. For example, for adiabatic flows and  $T_{\max}$  allowed to float to 28 keV, the continuum fit is poor, giving a reduced  $\chi^2 = 1.69$ . For a model where the  $\alpha$  index is permitted to float to its optimum value of 1.31, the fit is still poor,  $\chi^2 = 1.52$ .

Next we ran multiple-component optically thin thermal models with *mekal* for the five *XMM-Newton* spectroscopic cameras. The final results are shown in Table 4. These modeling results were similar to the results of S04 and L10 in that they led us

to an optically thin model with thermal plasma components and two absorption columns. The solution for the cool plasma component denoted by  $kT_2$  is an increase of 0.8 keV from the L10 model – a statistically significant result due to an actual spectral change according to our return to the L10 spectra with our *mekal* models. The addition of successive temperature components reduced the mean  $\chi^2$  from 1.70 to 1.48, to 1.28, and to (four components) 1.20. With each added component the improvement in fit over certain wavelength regions was marked. In particular, *mekal* models with fewer than four components also caused perceptible spurious undulating departures from the observed continua that were minimized with the inclusion of the fourth component. The addition of further components reduced the mean  $\chi^2$  by negligible amounts and were not significant according to statistical *f* tests performed in XSPEC. However, like L10 we were not able to fit both the pn/MOS and RGS spectra well unless we added a second column to attenuate the soft energies. We may parameterize our best *mekal* model with the equation:

$$\begin{aligned} phabs_a * & (mekal_1 + mekal_2 + mekal_3 + mekal_4) \\ & + phabs_b * (mekal_4 + gaussian), \end{aligned} \quad (1)$$

where the *mekal* subscripts 1–4 parameterize the temperatures  $kT_1$ – $kT_4$  of the four thermal plasma components of a 4-T model. The subscripts in *phabs* express the two independent column densities,  $n_{H_a}$  and  $n_{H_b}$ . As we will see, these values can be very different. We stipulate that it is possible in principle that the  $kT_{2-4}$  components could be represented in the  $n_{H_b}$  term as well, but their fluxes are so much weaker that we cannot solve for them as additional independent variables. In Fig. 5 we exhibit the unfolded model solution, including the normalizations, as an example for the range of 10–30 Å in OBS3. This gives a good feel for the relative contributions among the various plasma components for both the line and continuum spectra.

Figure 5 shows that even in the soft X-ray region the hot  $kT_4$  component dominates the flux. In Sect. 6.1 we noted that the hard/soft ratios can change over timescales of 100–1000 s. Despite the dominance of the hot emission component in the soft regime, the cool  $kT_1$  plasma can sometimes make its presence felt independently of the hot one. The most likely means for producing soft X-ray variability is for the line of sight column of matter to change to the hot emission sites behind it. If one assumes that the hot component fluxes decreased by free cooling,

<sup>4</sup> The differential emission measure for cooling flows is given by  $\text{DEM} = [(T/T_{\max})^\alpha](dT/T_{\max})$ . For adiabatic flows  $\alpha \equiv 1$ .

**Table 4.** Best parameters from X-ray Model of the form:  $(T_1 + T_2 + T_3 + T_4) * n_{H_a} + (T_4 + Gauss) * n_{H_b}$ .

Parameter	OBS1	OBS2	OBS3	OBS4
$n_{H_a}$ ( $10^{22}$ cm $^{-2}$ )	$0.133^{+0.001}_{-0.001}$	$0.124^{+0.001}_{-0.001}$	$0.090^{+0.001}_{-0.001}$	$0.128^{+0.001}_{-0.001}$
$kT_1$ (keV)	$0.115^{+0.002}_{-0.002}$	$0.110^{+0.002}_{-0.002}$	$0.104^{+0.001}_{-0.001}$	$0.111^{+0.002}_{-0.002}$
EM <sub>1</sub> ( $10^{55}$ cm $^{-3}$ )	0.14	0.10	0.21	0.12
$kT_2$ (keV)	$0.60^{+0.02}_{-0.02}$	$0.64^{+0.02}_{-0.02}$	$0.63^{+0.01}_{-0.01}$	$0.62^{+0.01}_{-0.01}$
EM <sub>2</sub> ( $10^{55}$ cm $^{-3}$ )	0.33	0.27	0.37	0.32
$kT_3$ (keV)	$3.63^{+0.22}_{-0.19}$	$4.30^{+0.22}_{-0.19}$	$4.20^{+0.14}_{-0.14}$	$3.43^{+0.13}_{-0.13}$
EM <sub>3</sub> ( $10^{55}$ cm $^{-3}$ )	0.18	0.29	0.45	0.22
$kT_4$ (keV)	$14.66^{+0.31}_{-0.39}$	$14.23^{+0.25}_{-0.22}$	$15.71^{+0.22}_{-0.23}$	$13.51^{+0.18}_{-0.16}$
EM <sub>4(<math>n_{H_a}</math>)</sub> ( $10^{55}$ cm $^{-3}$ )	3.0	2.6	3.5	2.6
EM <sub>4(<math>n_{H_b}</math>)</sub> ( $10^{55}$ cm $^{-3}$ )	0.7	1.0	0.8	0.7
$f_T$ (erg cm $^{-2}$ s $^{-1}$ )	$2.63 \times 10^{-10}$	$2.49 \times 10^{-10}$	$3.89 \times 10^{-10}$	$1.79 \times 10^{-10}$
$n_{H_b}$ ( $10^{22}$ cm $^{-2}$ )	$36.3^{+4.6}_{-3.3}$	$57.0^{+3.8}_{-4.2}$	$59.6^{+3.5}_{-2.6}$	$73.7^{+3.2}_{-3.0}$
redshift	0.0018	0.0005	0.0007	0.0003
$\chi^2/\text{d.o.f.}$	1.15/3189	1.18/2877	1.18/3663	1.20/3441

**Notes.** The following elemental abundances were fixed to nonsolar values:  $Z_{\text{FeK}\alpha} = 0.18 \times Z_{\text{Fe},\odot}$ ,  $Z_N = 2.33 \times Z_{N,\odot}$ ,  $Z_{\text{Ne}} = 1.8 \times Z_{\text{Ne},\odot}$ . Nonzero redshift values are not considered statistically significant because they are of the order of known seasonally-induced shifts in the instrument (e.g., Pollack 2010). Entries marked “ $f_T$ ” are unabsorbed fluxes in the energy range 0.2–12 keV.

i.e., proportional to the reciprocal of the density, this timescale gives an electron density of  $\sim 10^{11}$  cm $^{-3}$ .

Whereas components  $kT_2$  and  $kT_1$  are critical to the fits of lines of the Fe L-shell, N, and C ions, the  $kT_3$  component is the least stable in our solutions. One reason for including  $kT_3$  is that it easily produces the Fe XXV Ly $\alpha$  line and contributes to part of the continuum. However because the continuum flux spectrum of our  $kT_3$  runs parallel to the  $kT_4$  in a logarithmic plot (Fig. 5), it is possible that this component is an artifact of what is actually a continuous Differential Emission measure (DEM) parameterized by  $kT_4$  but extending down to a few keV. To test this possibility we ran an XSPEC add-on package written by Arnaud called *vgadem*, which is a DEM response shaped like a Gaussian, with a peak emissivity at 12.25 keV and a sigma of 5.47 keV. The values of the  $kT_1$  and  $kT_2$  were essentially identical with those determined with the *mekal* model. The resulting model replaces the monoenergetic emissivity terms,  $kT_3 + kT_4$ , in the parenthesis term of Eq. (1) and  $kT_4$  in the second term with one having a broad DEM. For our test case (OBS1) this model gave an acceptable  $\chi^2$  of 1.19 for the global fit. However, we found this solution to be unstable in convergence, and it slightly underpredicts the strength of the Fe XXVI line. In all, it does not perform as well as the *mekal* 4-T model over all wavelengths. We had a similar result running *vgadem* with the 2004 spectrum and abandoned this model. From these trials we could not corroborate our hypothesis that the  $kT_3$  plasma is an unnecessary product of our reference model.

We pursued this investigation by comparing our *mekal* 4-T and 3-T models and excising the wavelengths around the Fe XXV line. We found that the inclusion of the  $kT_3$  apart from these wavelengths causes the 4-T model to fit the continuum slightly better ( $\chi^2$  from 1.19 to 1.15). Thus, the  $kT_3$  in *mekal* seems needed for an ideal fit to the continuum too. However while introduction of the  $kT_3$  improves the fit for Fe XXV in our reference model, the fit for Fe XXVI is actually made slightly worse than for the reference model. To conclude, although we cannot provide an objective reason for preferring the 3-T *vgadem* DEM model over the reference model, the *mekal* model with  $kT_3 \approx 4$  keV actually appears not to be ideal either. We suspect a flatter DEM with cutoffs at low and high energies could improve

these fitting deficiencies. In fact, there are physical reasons for believing that the high energy source for the X-ray emissions of this star is not single-valued in energy even as there are reasons for suspecting that the “ $kT_3$  component” is in fact not independent of the  $kT_4$  one.

We give the parameters found in the *mekal* solutions represented by Eq. (1) in Table 4. The solution also stipulates the anomalous abundances found. Some 80% of the flux is emitted by a hot component we designate  $kT_4$ . This percentage increases to about 87% for the case that  $kT_3$  represents an extension of  $kT_4$ .

The  $kT_4$  component dominates emission at all wavelengths, so much so that it serves to weaken color ratio changes represented in Fig. 3 when the  $kT_4$  component alone does not vary. This emission also dilutes the equivalent widths (EWs) of some lines produced in cooler plasmas. Figure 5 shows the unfolded model RGS spectra for OBS4 from the 4-temperature model described in Table 4. We remind the reader that the  $kT_4$  flux is composed of a flaring and a dominant basal component.

### 6.3. Analysis of secondary parameters

*Column densities, abundances, and line broadening:* we list additional details emerging from our analysis:

- the  $n_{H_b}$  values are the largest documented to date and are a few times larger than the  $1 \times 10^{23}$  cm $^{-2}$  found by S04. The values change by  $\approx 2\times$  among the four spectra.
- the ratios of volumes associated with the “lightly absorbed” ( $n_{H_a}$ ) and “heavily absorbed” ( $n_{H_b}$ ) columns (given by the respective EMs in Table 4 and in tables in S04 and L10) remain the same during 2001, 2004, and 2010. From Table 4 these ratios are  $25^{+5}_{-15}\%$ ,  $23 \pm 3\%$ , and  $27 \pm 5\%$ , respectively.
- the *bvapec* task was used to determine abundances of elements from all the strong lines. Like several previous studies, the Fe abundance derived from the L shell ions is close to the solar value. The abundance determined from the two Fe K shell ion lines is  $0.18\times$  the solar value. This is statistically significantly higher than the even lower value of 0.12 found by L10. We used *bvapec* also to determine Ne and N abundances of 1.80 and 2.33 times solar, respectively,

from their Ly $\alpha$  line strengths. This is slightly more moderate than the  $2.63 \pm 0.78 \times$  and  $3.96 \pm 0.28 \times$  solar values that L10 found. We found no statistically significant changes in these abundances among the four 2010 observations.

- the XSPEC model *bvapec* was used on the strongest line profiles in the RGS spectra to determine Gaussian line broadening. Our solutions were dominated by the strong O VIII line. We found FWHM values in the range 540–950 km s $^{-1}$ . These values are marginally larger than the moderate values of 400 km s $^{-1}$  and 478 km s $^{-1}$  found by S04 and L10, respectively.
- Fe K and (barely) Si K fluorescence features are present. The EW of the Fe feature is  $-35\text{m}\text{\AA}$  to  $-50\text{m}\text{\AA}$ . Although these features were present in earlier high resolution spectra, their strengths in the 2010 spectra are the highest reported so far.

*Spectra derived from low and high flux time intervals:* In order to understand how key fitting parameters change when  $\gamma$  Cas's emission changes between low to high states (usually due to flaring), we split up the good time intervals according to low and high fluxes (relative to the means) and reconstructed spectra into low- and high- flux pairs. We discovered that the low and high flux times were strongly grouped together, creating split segments of times. The duration of these various segments was from 3–30 min. This timescale is longer than durations of flares.

The flux differences between these pairs were statistically significant, but only for the  $kT_4$  plasma component. Except for OBS1, the high-flux spectrum was several percent hotter than the low-flux one. The largest difference in the solution for the  $kT_4$  component occurred for OBS3. In this case the  $kT_4$  values for the high and low flux values were 16.08 keV and 14.59 keV, which, given the errors of  $\pm 0.59$  keV, is statistically significant at more than two sigma. (We repeated this experiment for the 2004 *XMM-Newton* observation by splitting it into two equal time segments and examining the low and high flux states in each half. We found no evidence for temperature differences for this observation.) Differences in the column densities between the pairs were not significant.

Even so, we found several statistically significant differences among the high-/low-flux spectra among several emission lines, most especially those arising from the Fe L shell ions, an emission feature at 16 Å (the wavelength of O VIII Ly $\beta$ ) and a neighboring Ne X line, and also a blend of the N VII Ly $\alpha$  and a nearby N VI line at 24.8 Å. The general pattern is that these lines are stronger in the low-flux spectra. To shed light on these changes, we constructed unfolded spectra for each of the 8 high/low-flux spectra (two for each one of the four observations), according to their normalizations. Examples of this unfolded low-flux spectrum for OBS3 are shown in Fig. 6. The prominence of these lines was actually due to a diminished dominance of the  $kT_4$  continuum, but not the lines, for the low spectrum fluxes. In other words, the spectra of all the cooler components then “peek through” the dominant continuum emitted by  $kT_4$ . The result is a highly dynamically changing spectrum. The details of the low/high flux spectrum differences can be summarized in the following:

- differences in strengths of most lines but O VIII, e.g., Fe L shell ions of Fe XVII and Fe XVIII, Ne X, and Fe XVIII-blended Ly $\beta$ /Ly $\alpha$ , especially in OBS2 and OBS3. The change is the smallest for O VIII Ly $\alpha$  because the  $kT_2$ ,  $kT_3$ , and  $kT_4$  plasma components contribute comparable amounts of EW. Therefore, changes among these components' normalizations, for example in the spectra extracted

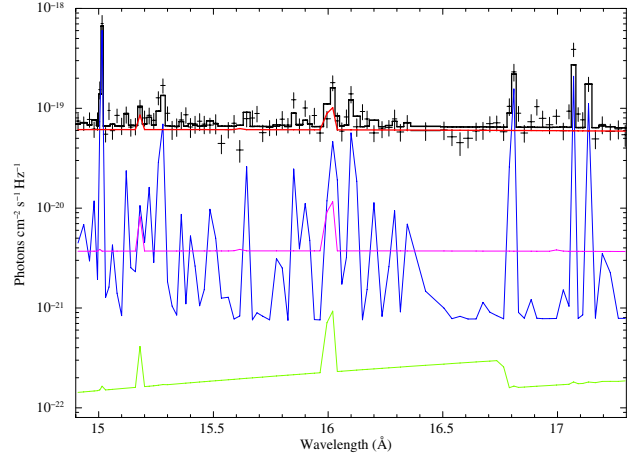


**Fig. 6.** Unfolded spectra for the spectral region shown in Fig. 7, for OBS3 (same color coding as in Fig. 5). Most of the lines arise from the L-shell ions of Fe XVII & XVIII. Note that the strengths of most lines depends on the normalization of the  $kT_2$  emission component (blue) relative to the dominant  $kT_4$  component (red).

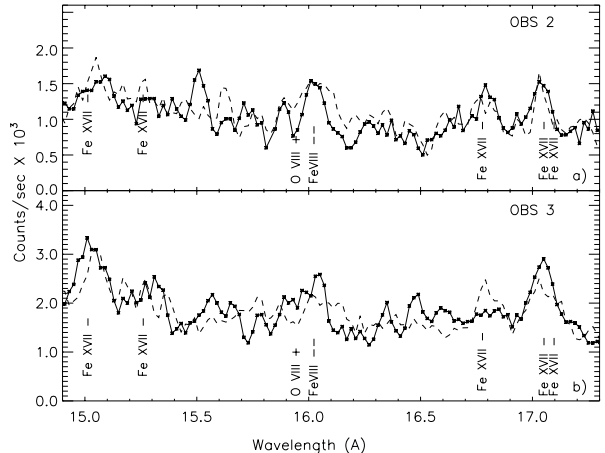


**Fig. 7.** *XMM-Newton/RGS* spectra obtained from high (dashed line) and low (solid) flux good time intervals in the 15–17 Å (Fig. 6) region in which several density-sensitive Fe XVII lines are present for OBS2 and OBS3. The generally greater strengths of these lines and the 16.8 Å/17.0 Å ratio are discussed in the text. These spectra are smoothed over two 2 mÅ bins.

from low and high fluxes, do not affect their equivalent widths significantly.

- analysis of unfolded spectra constructed from the high and low fluxes shows why these rapid variations in line strengths occur: the  $kT_4$  emission component in the low-flux spectrum decreases and allows emission from primarily the  $kT_2$  component to be more visible. An example is displayed in Fig. 7b and modeled in Fig. 6.

The change in  $n_{H_b}$  for low/high (OBS3) is of the same order as the deviations around the observational averages.

*Other lines and density diagnostics:* similar to S04 and L10, where the *fir* (forbidden/intercombinational/radiative) triplet complex is observed, in this case for N VI and O VII, we find that the ratio  $G \equiv (i + f)/r \approx 1$ , and this means that the dominant process for formation of these triplet lines is consistent with the dominance of collisions in determining the relative level populations. Likewise, we find the ratio  $f/(i + r) \sim 0$ . This might be explained by the metastability of the upper level ( $1s2s\ ^3S_1$ ) of

the forbidden transition. However, it is at least as likely that this level is radiatively depopulated by intense UV flux from a nearby hot star, in which case the utility of the forbidden component as a density diagnostic is vitiated. Thus, as with the former studies, we cannot draw conclusions about density from these features.

Other density-sensitive diagnostics are available among several Fe XVII lines at wavelengths accessible to both the *Chandra*/HTEG and *XMM-Newton*/RGS wavelength regions. These have been studied empirically and theoretically in detail by Mauche and collaborators (Mauche et al. 2001, 2004) in the well observed *Chandra*/HTEG spectra of the mCV (polar) star AE Aqr. The lines in this source appear to be emitted in plasma with thermal conditions similar to those of the  $kT_2$  plasma of  $\gamma$  Cas. The ratios formed by these line strengths are more useful for these purposes than the *fir* triplets because the atomic level populations are found to be affected by UV photoexcitations by only  $\approx 10\%$  or less (Mauche 2002).

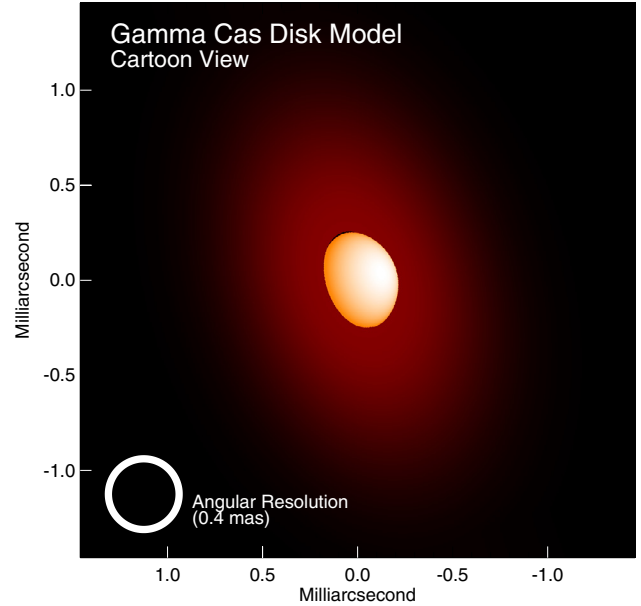
In the competition between radiative and collisional deexcitations of the upper atomic levels, high densities mainly affect the lines arising from transitions from the lowest member of an excited manifold. For the resonance Fe XVII lines we can observe these terms of these manifolds correspond to the  $2p^53d$  and  $2s^23s$  terms. The observable transitions most affected are 15.26 Å and 17.10 Å, respectively. Both of these are too weak to be used in our analysis, so we must resort to alternative diagnostics.

Figure 7 exhibits the principal Fe XVII ion lines visible in the 15–17 Å region. The spectra shown are averages of features recorded in both RGS cameras and smoothed over two wavelength bins. The line ratio formed by 17.10 Å (magnetic quadrupolar transition) and 17.05 Å is a density diagnostic (Klapisch et al. 1978; Mauche et al. 2001). We estimate that in our spectra the ratio  $I(17.1\text{ \AA})/I(17.05\text{ \AA})$  lies in the range of 0.0–0.4 (with a value near zero most likely). This means that the electron density is of order  $10^{14}\text{ cm}^{-3}$  or higher, according to Mauche et al. (2001). For OBS2 the ratio  $I(16.8\text{ \AA})/I(17.0\text{ \AA}) \approx 1$ . From the work of Mauche et al. this ratio implies a density near  $10^{13-14}\text{ cm}^{-3}$  for both the high-flux and low-flux spectra. However, for OBS3 this same ratio has values  $\approx 1$  for the high flux spectrum and decidedly less than 1 for the low flux spectrum. The last ratio indicates  $N_e \gtrsim 10^{14}\text{ cm}^{-3}$ . (This same condition occurs for both the low and high spectra of OBS4, although it is not shown.) This difference suggests that the densities of the emitting plasma can sometimes fluctuate even on timescales of several minutes. Moreover, that the low-flux spectra constructed from any of the other observations shows no comparable weakness of 16.78 Å and that the higher density range is more typical. Altogether, the Fe L ion lines suggest high densities for the  $kT_2$  plasma component. These electron densities are centered near  $10^{14}\text{ cm}^{-3}$  and can fluctuate around a mean value of  $10^{13-14}\text{ cm}^{-3}$  on either short or long timescales. The densities for this plasma component are similar to those found for the high temperature flares from independent plasma cooling arguments (SRC). This high density constitutes one of the more surprising results we have found in this study.

## 7. Discussion

### 7.1. Connections to the circumstellar environment

Our analysis of CHARA MIRC and VEGA data resulted in similar disk solutions. There is also an indication that matter may be dispersed beyond the disk and is visible in the near-IR. As for the disk itself, its extent is larger in the *H*-band than the *R*-band



**Fig. 8.** Artistic rendition depicting the IR *H*-band emission determined for  $\gamma$  Cas. We show the derived extent, elongation, and position angle of the Gaussian disk. The inner region is optically thick. Neither partial obscuration of the star by the disk nor the star's gravity-darkening are included in the MIRC model.

(near  $\text{H}\alpha$ ), which is consistent with the higher disk opacity expected in the *H*-band.

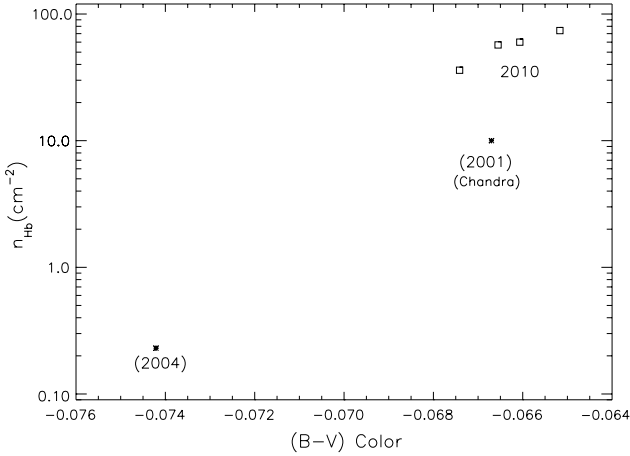
In addition, only the MIRC ring model gave acceptable errors. Certainly, a ring model cannot be ruled out from our study. However, if future LBOI work demonstrates that the disk reaches the star, this result will have to be reconciled with the presence of spectral *msf* and brief UV continuum light dips. These signal the presence of corotating structures close to the Be star. It would seem that shear forces would destroy a high density structure in a transition zone between corotating regions and a Keplerian disk extending inward that intrudes upon them. Thus, we expect the shears would force the inner disk transition to evolve to a ring structure. It may be important that Hony et al. (2000) found that the weak Brackett emission lines in the  $\gamma$  Cas spectrum are broadened to  $\approx 550/\sin i\text{ km s}^{-1}$  and gave arguments why the broadening is most likely kinetic. This velocity is significantly above the projected stellar rotation rate. This inference could be further evidence of corotating matter close to the star. In the event that the disk touches the star, the corotating clouds would have to lie elsewhere, e.g., outside the disk plane at intermediate latitudes.

Figure 8 gives a feel for the geometry of the system viewed from our vantage point. Models derived from LBOI are sufficient to describe the relative contributions of the  $\gamma$  Cas star/Be disk system. They indicate that its disk contributes 22% to the *V* band brightness and only 3–4% in *B*, of the star-disk system (Stee & Bittar 2001). (Note that this prediction depends on disk conditions observed in 1993 and on assumptions about the disk-photosphere transition.) The *B* – *V* color variations in Fig. 1a confirm these predictions. The Be disk is the only practical place in the system where secular and irregular continuum flux variations can originate in visible wavelengths. Moreover, the season-to-season averages shown in Fig. 1a have a linear regression slope  $\Delta B/\Delta V = 0.66 \pm 0.02$ . This slope is consistent with color/brightness ratio changes observed when disks of classical Be stars evolve in time (e.g., Hirata 1982).

**Table 5.** Density columns (in  $10^{22} \text{ cm}^{-2}$ ), Gaussian  $EW$  of Fe fluorescence, abundance anomalies (solar; Fe refers to K-shell).

Date	Binary phase	$n_{H_b}$	$EW(\text{FeK})$ (mÅ)	Fe	Ne	$N$
2001	0.75	10	-19	0.10	~1	~1
2004	0.27	0.23	-10	0.12	2.63	3.96
2010	0.74–0.96	36–74	-35 to -50	0.18	1.80	2.33

**Notes.** “Fe” refers to Fe abundance from K-shell ion lines. Errors for [Fe], [N], and [Ne]:  $\pm 0.02$ ,  $\pm 0.75$ , and  $\pm 0.28$ , resp.



**Fig. 9.** The APT-measured  $B - V$  colors corresponding to the epochs of the six  $n_{H_b}$  absorption columns determined from soft X-ray flux attenuations. The  $n_{H_b}$  values increased monotonically during 2010. The errors in determining  $n_{H_b}$  are  $\pm 10\%$ .

In Sect. 6.2 we reported that during the 44 day interval of our 2010 observations the  $n_{H_b}$  column increased by about a factor of two. This rate of increase defines the column at which this range can change with time. Altogether a change of  $300\times$  has been found between 2004 and 2010. As already stated, our observations covered the orbital interval between inferior conjunction (Be star closest to the Sun) and RV maximum. The orbital phase (0.75) at which *Chandra* observed the large  $n_{H_b}$  in 2001 was almost identical to the phase of our first 2010 observation (0.74). Although it was still high in 2001, this column was smaller than in any of the 2010 observations. As the *XMM-Newton* sequence progressed toward quadrature, the  $n_{H_b}$  became higher yet. These values are summarized in Table 5.

From this it is difficult to maintain that changes seen in  $n_{H_b}$  in 2010 can be attributed primarily to binary phase. If they do correlate with phase it must be in a complicated manner. Instead, as indicated in Table 5,  $n_{H_b}$  absorption correlates strongly with the reddening. We exhibit this relation in Fig. 9. This plot shows that the relation exists not just for the 2001 and 2004 observations but also for the four in 2010. Since we have associated reddening with disk development, this figure suggests that an association exists between X-ray absorption and disk conditions.

We also find in Table 5 a suggestion of temporal variance between the  $n_{H_b}$  column and the strengths of the Fe fluorescence feature, the K-shell-derived abundance of Fe, and of [N] and [Ne]. It appears that the status of the Be disk is related to several peculiar properties of the X-ray emitting plasma.

Although it is by no means clear how these physical parameters are connected, one might begin to connect the dots by noting that the smaller than unity ratios of  $\Delta B/\Delta V$  observed by the APT

are likely caused by the Be star injecting matter into its surroundings. In fact, variations in  $V$  and  $B$  of 0.015–0.025 mag over several hours have been observed on a few occasions (SHV). During these events the ratios of the  $\Delta B/\Delta V$  were typically 0.85–90, i.e., grayer than longer term variations as recorded in Fig. 1a. Such events suggest a highly dynamic environment in some places over the Be star, perhaps as associated with failed local ejections or magnetic prominences.

For more successful ejections to be associated with the  $n_{H_b}$  column, the ejections must: i) occur in lines of sight subtending a portion of the Be star; ii) be sustained over weeks or months; and iii) have a sufficient density that the emission measure ( $N_e^2$  integrated over volume) be visible in continuum light. For this study we cannot confirm the validity of these conditions from spatial models because our LBOI observations are made in optically thick wavelengths and thus do not measure changes in volumetric density. In consideration of ii) (sustainment), observations of  $\gamma$  Cas in the IUE archives at MAST<sup>5</sup> disclose that historically this star often alternated between prolonged periods of strong and weak states of the wind emanating from the Be star, with short transitions of 1–3 months between them. Generally, though not always, the  $H\alpha$  emission  $EWs$  were found to correlate with the wind state for  $\gamma$  Cas and other Be stars (e.g., Doazan et al. 1983, 1987). Therefore, it may be that the 2010 event we have reported for this star is one such “wind” episode. We also note that there is a discrepancy between the range found in the optical depths of the UV resonance lines and the larger range of  $n_{H_b}$  values. Lacking a new opportunity for simultaneous UV-X-ray observations of  $\gamma$  Cas, a resolution of this issue is not at hand.

We make no assumption about what ejection mechanism might be responsible for the mass loss or tossing episodes. As suggested in Sect. 2, a wind driven by radiative and centrifugal forces alone may play a role in this, but if so it is likely to be modified by additional processes that are not identified among classical Be stars. One attribute in the  $\gamma$  Cas wind not found in others is a “flickering” in the violet wing of the Si IV and C IV resonance lines on a timescale of  $7\frac{1}{2}$  h (Cranmer et al. 2000; “CSR”). This timescale is also seen in the X-ray flux of this star. CSR suggested that the rotation into view of X-ray active centers on the Be star increases the local wind ionization, thereby causing optical depth changes but not otherwise influencing the wind structure or mass loss rate. Whatever the cause, disk diagnostics would be influenced by changes in the geometry and instantaneous rates of the outflows. Even so, these might not change the strength of the X-ray Fe-K fluorescence feature (formed by a wide range of Fe ions) and certainly not the Fe, N, and Ne abundance anomalies. Although none of this is understood, it is at least clear now that these abundances can vary on timescales of 1–2 years in the X-ray emitting plasma. This result cannot be understood as a result of recent nucleosynthetic processing in the stellar interiors.

All three high resolution X-ray studies of this star have found it necessary to include two absorption columns into the X-ray fitting models. This raises the question of why it is that no matter what the  $n_{H_b}$  column density happens to be at any one time, it includes only the same fraction, 23–27%, of the X-ray emitting volumes. We can address this question by supposing that the X-rays are emitted on or very near the surface of the Be star from a confined range of latitudes. One can then imagine that as

<sup>5</sup> “MAST” represents the Multi-Mission Archive at the Space Telescope Science Institute (STScI). Support for MAST is provided by NASA Office of Space Science via grant NAS5-7584.

the flow escapes and crosses our line of sight it will clear all but the “lower” portion of the stellar disk. The lower region of the star covered by this outflow, perhaps 25%, would be the X-ray emission volume suffering the  $n_{H_b}$  absorption. In this picture the fraction of the disk obscured by the column would be some function of the confinement of the outflow in latitude, the inclination of the star and Be disk, the oblateness of this very rapidly rotating star, and the separation of the inner edge of the Be disk from the star. With the right selection of parameters the areal coverage fraction of the  $n_{H_b}$  column can remain approximately constant.

Our picture must be confronted with additional optical photometry and X-ray spectra. The predictions for  $\gamma$  Cas are clearly that sudden brightness increases and  $B - V$  reddening should continue to be *simultaneously* accompanied by increased amounts of expelled particles. A portion of the released matter, perhaps this is an episodic wind, is directly observable in the soft X-ray domain by its effect on this flux. If verified, this picture promises to be more evidence that some, and by implication all, of the hard X-ray flux of  $\gamma$  Cas is created close to and in front of the Be star.

## 7.2. A $kT_1$ -wind connection?

Our analyses of the X-ray spectra have not been able to clearly identify the location of the formation of the secondary ( $kT_1 - kT_3$ ) plasma components. The Fe L-shell ion line ratios yield high density for the  $kT_2$  component, implying that it is formed near the primary  $kT_4$  emission source. As to the cool  $kT_1$  component, L10 discussed the pro’s and con’s of whether it is associated with the standard wind of single hot stars. Their conclusion was the EM1 of this component is larger than found for standard winds but its temperature is consistent with them. In this work we can take this conclusion one step further by pointing out that at least some of the slow  $I_{2-10 \text{ keV}}/I_{0.3-2 \text{ keV}}$  X-ray color variations shown in Fig. 3 arises from the soft energy band for which  $kT_1$  is an important contributor. Because rapid fluctuations have not been reported from X-rays originating from shocks in B star winds, we believe this component does not arise primarily from winds:  $kT_1$  is somehow part and parcel of the X-ray generation processes in  $\gamma$  Cas.

## 8. Conclusions

This study combines contemporaneous information obtained by a multidisciplinary campaign on a complicated  $\gamma$  Cas system (Be star + binary orbit + Be disk). We have refined its orbital ephemeris: it is in a nearly circular orbit with  $P_{\text{orb}} \approx 203.53$  days. We also confirmed the Meilland et al. (2007b) result using new LBOI observations in  $H\alpha$  light that the  $H\alpha$ -emitting disk rotates at a rate consistent with Keplerian rotation. Its extent has been traced out to about one half the Be star’s Roche lobe radius. We find from optical spectroscopy and imaging that there is no longer evidence of a visible one-armed disk structure. Moreover, the  $V$  and  $R$  emission components in the  $H\alpha$  line are weaker than before the year 2000. These changes are not atypical in the context of the behavior of Be disks.

Yet in other respects  $\gamma$  Cas’s recent history is not typical. The APT record shows an abnormal rate of brightening and reddening of  $\gamma$  Cas, and there can be little doubt that this is caused by the interaction of newly ejected particles with the disk. Such events are often observed in monitoring Be stars, so this can have little to do with the star’s binarity or the fact that it emits copious X-rays. Fortunately, the activity the APT recorded also coincided with the onset of our four XMM observations. As stated

in Sect. 6.2 the attenuation of soft X-ray flux is caused by an increase in a column density  $n_{H_b}$  that covers  $\frac{1}{4}$  of X-ray emitting sites. The rate of increase in  $n_{H_b}$  during the 2010 observations is consistent with the changes in  $n_{H_b}$  measured in 2001 and 2004. These column densities in turn are correlated with the changes in the  $V$  magnitude and  $B - V$  color but are not related in a simple way to orbital phase. We argued that the logical place for the  $n_{H_b}$  to originate is from the time-dependent efflux from the Be star. We noted that these variations occurred without the additional variable column provided by a 1-armed disk structure. X-ray studies during the precession of a future V/R cycle could test conclusively whether the  $n_{H_b}$  variations are associated with the central Be star.

Certain other aspects of the X-ray emitting plasma discussed in L10 are also clearer than before. The multi-thermal component nature of the sites seems relatively stable. We stress that the soft X-ray flux from the hot  $kT_4$  component dominates the contributions of the cooler components. Even so, one can still see that the electron densities of the warm plasma component are high, probably  $10^{13} \text{ cm}^{-3}$  or more. The cool X-ray plasma component clearly forms in different volumes but seems to have a higher emission measure, even in 2004, than is expected for a typical wind of an early B star. In addition, we noted that the soft X-ray flux sometimes exhibits rapid aperiodic variations. This is not a known characteristic of Be star winds.

From the correlation between color, and X-ray column density shown in Fig. 9, it is reasonable to conclude that  $\frac{1}{4}$  (all?) of the hot X-ray sites lie within a high density ( $\gtrsim 10^{14} \text{ cm}^{-3}$ ) medium like the photosphere of a star and the observer. In principle, an alternative interpretation is that the figure represents statistical flukes. A second alternative is that the column density represented by  $n_{H_b}$  is associated with accretion onto a dense column above a degenerate companion. There are difficulties associated with this picture, one of which is the faithful response of particle densities in the downstream column to an input variation far upstream in the Be wind. The picture would assume that the variations in the wind, the dense inner regions of the Be disk where the  $V$  flux is formed, and infall to a secondary some distance away, are all synchronized, with at most a short delay. Even assuming this chain of events offers no obstacles, such a picture would have to confront the correlations of rapid variations between X-ray and UV continuum and line fluxes expected to be visible only in the vicinity of the Be star.

Aside from its correct interpretation, the reddening-column correlation promises for the first time to predict readily observable changes in X-ray properties of  $\gamma$  Cas. It will be interesting to see with a future instrument if this relation extends to the column densities, abundances, and fluorescence strengths found for other  $\gamma$  Cas members.

**Acknowledgements.** The quality of this paper was greatly improved by discussions with Dr. Maurice Leutenegger. We want to also express our appreciation to Drs. J. Nemravová and P. Harmanec and collaborators for sending us their manuscript on RVs in  $\gamma$  Cas in advance of publication. Dr. Harmanec’s insights improved the quality of the paper. Dr. J. Nemravová’s updates on the status of Ondrejov H $\beta$  observations filled in an important historical gap. This work has made use of the BeSS database, operated at LESIA, Observatoire de Meudon, France: <http://basebe.obspm.fr>. We also wish to thank the valuable comments by the referee, especially concerning additional interpretations of the wind-disk interaction. This work was supported in part by NASA Grant NNX11AF71G. RLO acknowledges financial support from the Universidade Federal de Sergipe through the MAGIS Program, and also from the Brazilian agency FAPESP (Fundação de Amparo à Pesquisa do Estado de São Paulo) through a Young Investigator Program (#2009/06295-7 & #2010/08341-3). The latter allowed the development his work on this study during his stay in the Instituto de Física de São Carlos of the Universidade de São Paulo and visit to

the United States. G.W.H. acknowledges support from NASA, NSF, Tennessee State University, and the State of Tennessee through its Centers of Excellence program.

## References

- Balona, L. A. 2009, in Stellar Pulsation: Challenges for Theory & Observation, AIP Conf. Ser., 1170, 339
- Balona, L. A., Pigulski, A., Cat, P. D., et al. 2011, MNRAS, 413, 2403
- Berio, Ph., Stee, Ph., Vakili, F., et al. 1999, A&A, 354, 203
- Brown, J. C., Cassinelli, J. P., & Maheswari, M. 2008, ApJ, 688, 1320
- Carciofi, A. C. 2011, in Active Be Stars, IAUS, 272, 325
- Carciofi, A. C., Bjorkman, J., Otero, S. A., et al. 2012, ApJ, 744, L15
- Che, X., Monnier, J. D., Webster, S., et al. 2010, Proc. SPIE, 7734, 91
- Clark, J. S., Tarasov, A. E., Okazaki, A. T., et al. 2001, A&A, 365, 629
- Collier Cameron, A., & Robinson, R. D. 1989, MNRAS, 238, 657
- Cowley, A. P., Rogers, L., & Hutchings, J. B. 1976, ApJ, 88, 911
- Crammer, S. R., Smith, M. A., & Robinson, R. 2000, ApJ, 537, 433 (CSR)
- Delaa, O., Stee, Ph., Meiland, A., et al. 2011, A&A, 529, A87
- Doazan, V. 1982, in B Stars with and without Emission Lines, NASA SP-456, 325
- Doazan, V., Franco, M., Sedmak, G., Stalio, R., & Rusconi, L. 1983, A&A, 128, 171
- Doazan, V., Rusconi, L., Bourdonneau, B., Sedmak, G., & Thomas, R. N. 1987, A&A, 182, L25
- Donati, J.-F., Collier Cameron, A., Hussain, G. A. J., et al. 1999, MNRAS, 302, 437
- Dziembowski, W., Dzynńska, J., & Pamyatnykh, A. 2007, Commun. Asteroseismol., 150, 213
- Feinstein, A., & Marraco, H. G. 1979, AJ, 84, 1713
- Frémant, Y., Zorec, J., Hubert, A.-M., et al. 2005, A&A, 440, 305
- Gies, D. R., Bagnuolo, W. G., Baines, E. K., et al. 2007, ApJ, 654, 527
- Güdel, M., & Nazé, Y. 2009, A&AR, 17, 309
- Harmanec, P. 2002, Exotic Stars as Challenges to Evolution, ed. C. A. Tout, & W. Van Hamme, 279, 221
- Harmanec, P., Habuda, P., et al. 2001, A&A, 364, L85
- Henrichs, H. F., Hammerschlag-Hensberge, G., & Howarth, I. D. 1983, ApJ, 268, 807
- Hirata, R. 1982, in Be stars (Dordrecht: Reidel Publ.), IAU Symp., 89, 41
- Hony, S., Waters, L. B., Zaal, P. A., et al. 2000, A&A, 355, 187
- Horaguchi, T., Kogure, T., Hirata, R., et al. 1994, PASJ, 46, 9
- Hummel, W. 2000, in The Be Phenomenon in Early Type Stars, ed. M. A. Smith, H. F. Henrichs, & J. Fabregat, ASP Conf Ser., 214, 396
- Itoh, K., Okada, S., Ishida, M., Kunieda, H., et al. 2006, ApJ, 639, 397
- King, A. R., & Watson, M. G. 1987, MNRAS, 227, 205
- Lopes de Oliveira, R., & Motch, C. 2011, ApJ, 731, L6
- Lopes de Oliveira, R., Motch, C., Haberl, F., Negueruela, I., & Janot-Pacheco, E. 2006, A&A, 454, 265
- Lopes de Oliveira, R., Smith, M. A., & Motch, C. 2010, A&A, 512, A22 (L10)
- Lucy, L. B. 2005, A&A, 439, 663
- Marco, A., Negueruela, I., & Motch, C. 2007, ASP Conf Ser. 361, ed. S. Stefl et al., 388
- Marco, A., Motch, C., Negueruela, I., et al. 2009, AdSpR, 44, 348
- Mauche, C. W. 2002, The Physics of Cataclysmic Variables & Related objects, ed. B. T. Gritsche, et al., ASP Conf. Ser., 261, 113
- Mauche, C. W. 2009, ApJ, 706, 130
- Mauche, C. W., & Liedahl, D. A. 2001, ApJ, 560, 992
- Mauche, C. W., & Liedahl, D. A. 2004, UCRL-PROC-208729
- Meiland, A., Millour, F., Stee, P., et al. 2007a, A&A, 464, 73
- Meiland, A., Stee, Ph., Vannier, M., et al. 2007b, A&A, 464, 59
- Miroshnichenko, A. S., Bjorkman, K. S., & Krugov, V. D. 2002, PASP, 114, 1226
- Monnier, J. D., Berger, J., Pedretti, E., et al. 2008a, Proc. SPIE, 5491, 1370
- Monnier, J. D., Zhao, M., Pedretti, E., et al. 2008b, Proc. SPIE, 7013, 1
- Morby, C. L., & Brosterhus, E. B. 1974, PASP, 86, 455
- Mourard, D., Bosc, I., Labeyrie, A., Koechlin, L., & Saha, S. 1989, Nature, 342, 520
- Mourard, D., Clausse, J. M., Marcotto, A., et al. 2009, A&A, 508, 1073
- Mukai, K., Kinkhabwala, A., Peterson, J. R., Kahn, S. M., & Paerels, F. 2003, ApJ, 586, L77
- Murakami, T., Koyama, K., et al. 1986, ApJ, 310, L31
- Neiner, C., de Batz, B., Inoue, H., & Agrawal, P. C. 2011, AJ, 142, 149
- Nemravová, J., Harmanec, P., Koubska, P., et al. 2012, A&A, 537, A39
- Ochsenbein, F., & Halbwachs, J. L. 1982, A&AS, 47, 523
- Okazaki, A. 1991, PASJ, 43, 75
- Okazaki, A., & Negueruela, I. 2001, A&A, 377, 161
- Pedretti, E., Monnier, J., Brummelaar, T. T., & Thureau, N. D. 2009, New A Rev., 53, 353
- Peters, G. P. 1982, PASP, 94, 157
- Peters, G. P. 1986, ApJ, 301, L61
- Pollack, A. 2010, Calibration status of XMM-Newton RGS, [http://xmm.esa.int/external/xmm\\_user\\_support/usersgroup/20100512/rgs\\_calib.pdf](http://xmm.esa.int/external/xmm_user_support/usersgroup/20100512/rgs_calib.pdf)
- Porter, J. M., & Rivinius, T. 2003, PASP, 115, 1153
- Quirrenbach, A., Bjorkman, K. S., Bjorkman, J. E., et al. 1997, ApJ, 479, 477
- Rakowski, C. E., Schulz, N. S., Wolk, S. J., & Testa, Paola 2006, ApJ, 649, L111
- Rivinius, Th., Baade, D., & Stefl, S. 2003, A&A, 411, 229
- Rivinius, Th. 2007, in Active OB stars, ed. S. Stefl, S. P. Owocki, & A. T. Okazaki, ASP Conf. Ser., 361, 219
- Robinson, R. D., & Smith, M. A. 2000, ApJ, 540, 474
- Robinson, R. D., Smith, M. A., & Henry, G. W. 2002, ApJ, 575, 435 (RSH)
- Safi-Harb, S., Ribo, M., Butt, Y., et al. 2007, ApJ, 659, 407
- Shafter, A. W., Szkody, P., & Thorstenson 1986, ApJ, 308, 765
- Slettebak, A., & Snow, T. P. 1978, ApJ, 224, L927
- Smith, M. A. 1986, ApJ, 304, 728
- Smith, M. A. 1995, ApJ, 442, 812
- Smith, M. A., & Balona, L. B. 2006, ApJ, 640, 491 (SB06)
- Smith, M. A., & Robinson, R. D. 1999, ApJ, 517, 866
- Smith, M. A., & Robinson, R. D. 2003, Interplay of Periodic, Cyclic, & Stochastic Variability in Selected Areas of the H-R Diagram, ed. C. Sterken, ASP Conf. Ser., 292, 263
- Smith, M. A., Peters, G. J., & Grady, C. A. 1991, ApJ, 367, 302
- Smith, M. A., Robinson, R. D., & Corbet, R. H. D. 1998a, ApJ, 503, 577 (SRC)
- Smith, M. A., Robinson, R. D., & Hatzes, A. P. 1998b, ApJ, 507, 945 (SRH)
- Smith, M. A., Cohen, D. H., Gu, M. F., et al. 2004, ApJ, 600, 972 (S04)
- Smith, M. A., Henry, G. W., & Vishniac, E. 2006, ApJ, 647, 1375 (SHV)
- Stee, P., & Bittar, J. 2001, A&A, 367, 532 (SB)
- Stee, P., & Mourard, D. 2012, A&A, submitted (Paper II)
- Stee, P., Vakili, F., Bonneau, D., Mourard, D., et al. 1998, A&A, 332, 268
- Tallon-Bosc, I., Tallon, M., Narusawa, S.-Y., et al. 2008, Proc. SPIE, 7013, 44
- Tanaka, K., Sadakane, K., Zavala, R. T., et al. 2007, PASJ, 59, L35
- Telting, J., & Kaper, L. 1994, A&A, 284, 515
- Tycner, C., Gilbreath, G. C., Zavala, R. T., et al. 2006, AJ, 131, 2710
- Walker, G. A. H., Kuschnig, R., Matthews, J. M., et al. 2005, ApJ, 635, L77
- Welsh, W., Horne, K., & Gormer, R. 1993, ApJ, 410, L39
- White, N. E., Swank, J. H., Holt, S. S., et al. 1982, ApJ, 263, 277
- Wynn, G. A., King, A. R., Horne, K., et al. 1997, MNRAS, 286, 436
- Yang, S., Ninkov, Z., & Walker, G. A. 1988, PASP, 100, 233